Electrostatic Potential Shielding in Representative Cislunar Regions

Kaylee Champion and Hanspeter Schaub

***Abstract*— Touchless potential sensing of neighboring spacecraft using photoemissions and secondary electron emissions has been investigated for geosynchronous (GEO) applications. As more missions are being sent to cislunar space, this technology may be extended there as well. However, the complexity of the cislunar environment presents novel challenges for touchless potential sensing technology. A chief issue is shorter Debye lengths than in GEO regions, which can be as low as 10 m in the cislunar regions. Therefore, a model for the electric and potential fields surrounding a charged spacecraft in short Debye regions around the moon is investigated. The vacuum (Laplace) and Debye–Hückel models are presented and effective Debye lengths are used to expand the models and better represent the environment. The effective Debye length has previously been investigated in low Earth orbit (LEO), quiet GEO, and asteroid environments but has not been found in the cislunar plasma environment, and a larger effective Debye length may allow touchless potential sensing using electron emissions to be possible at farther, safer distances than expected. Once the effective Debye lengths and associated models are established, the relationship between effective Debye lengths and touchless potential sensing capabilities is explored through computations in NASCAP-2k, a spacecraft–plasma interaction software. The developed methods are then used to determine whether passive and active touchless potential sensing is feasible in cislunar regions with nonnegligible electrostatic potential shielding.**

***Index Terms*— Electrostatic analysis, plasma, spacecraft charging, space environment.**

I. INTRODUCTION

NOVEL active and passive potential sensing of neighboring spacecraft has been investigated in recent years and deemed feasible for application the geosynchronous (GEO) region [1], [2], [3], [4]. Active potential sensing involves a servicing spacecraft directing an electron beam at a target so that secondary electrons [5], [6] and X-rays [7], [8] are emitted from the surface, as shown in Fig. 1. The use of a low-wavelength ultraviolet laser has also been investigated as a means to excite photoemissions from a target [9]. Secondary electrons and photoelectrons are emitted with low energies, so when they reach the servicer, they have been accelerated approximately to the potential difference between the servicer and the target. The incoming signals are then measured, and the servicer utilizes the measurements to infer the potential of the target with respect to its own potential. Passive potential sensing works in a similar manner, but instead of exciting emissions with an electron beam, natural emissions, including secondary electron and photoelectron emissions, caused by the ambient space and plasma environment are measured. Knowledge of a target's potential can be used to account for electrostatic perturbations during docking [10], [11] and minimize the risk of discharges during close proximity operations [12]. Awareness of a target's potential is also the first step toward electrostatic actuation. This may be implemented by a servicer, which aims an electron beam at a target, imposing a negative potential on the target and a positive potential on itself. This proposed implementation, deemed the electrostatic tractor, can be used to detumble or reorbit uncooperative targets or debris, dock incoming bodies, and conduct touchless in situ servicing [13], [14].

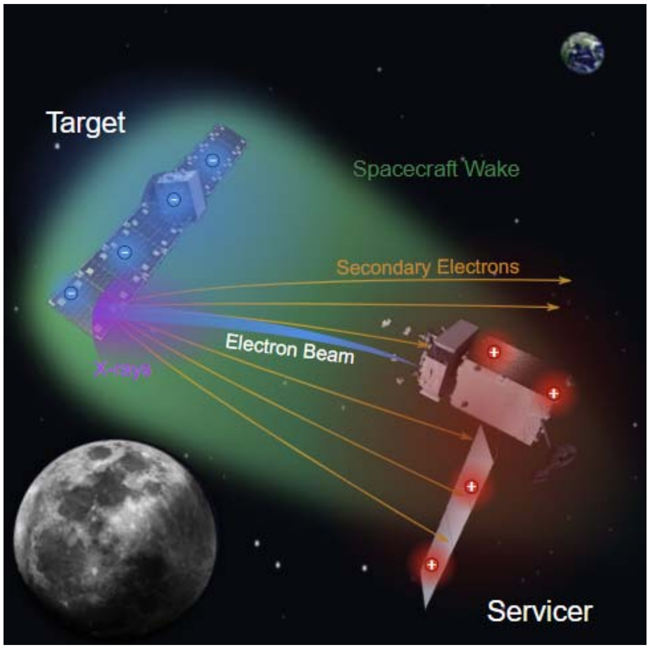

Fig. 1. Touchless potential sensing in cislunar space concept.

Manuscript received 22 August 2022; revised 8 November 2022; accepted 23 December 2022. Date of publication 25 January 2023; date of current version 12 October 2023. This work was supported in part by the NASA Space Technology Graduate Research Opportunity, in part by the U.S. Air Force Office of Scientific Research under Grant FA9550-20-1-0025, and in part by the National Science Foundation Graduate Research Fellowship. The review of this article was arranged by Senior Editor S. T. Lai. *(Corresponding author: Kaylee Champion.)*

The authors are with the Aerospace Engineering Sciences Department, University of Colorado at Boulder, Boulder, CO 80303 USA (e-mail: Kaylee.Champion@colorado.edu; Hanspeter.Schaub@colorado.edu).

Color versions of one or more figures in this article are available at https://doi.org/10.1109/TPS.2023.3236246.

Digital Object Identifier 10.1109/TPS.2023.3236246

An increasing number of missions have been sent and are scheduled to be sent to the cislunar region, such as NASA's twin ARTEMIS spacecraft, China's Chang'E-1 spacecraft, and the Lunar gateway [15], [16], [17]. In addition, one of NASA's strategic goals is to extend human presence to the moon and eventually Mars for sustainable long-term exploration, development, and utilization [18]. Spacecraft charging concerns persist around the moon, and touchless potential sensing may be extended to cislunar space as a result. However, the complexity of the cislunar environment presents novel challenges for touchless potential sensing technology. The focus of this study is the impact of short Debye lengths, as Debye lengths as low as ten meters are encountered in cislunar space. The Debye length is a measure of how far a charge's electrostatic effect persists, so short Debye lengths may limit the distance at which a servicer has electrostatic interactions with a target and distances at which a servicer can sense the potential of a target. Touchless potential sensing is intended for separation distances of 10–30 m [3], [19], [20], so a Debye length less than approximately 30 m is considered short. This has not posed an issue in GEO, as the Debye length there is typically up to several hundred meters, so potential shielding due to the ambient plasma is not considered a limiting factor in GEO [21], [22]. Therefore, the effective Debye length in regions around the moon is investigated. The effective Debye length more accurately represents potential and electrostatic shielding in plasma and may be several times larger than the Debye length [23]. Effective Debye lengths have been investigated around asteroids in interplanetary space [24], in a quiet GEO environment, and low Earth orbit (LEO) environments [19], but have not been investigated in cislunar space.

The goals of this work are to investigate limitations on servicer–target electrostatic interactions and touchless potential sensing due to the ambient plasma environment in cislunar space regions and determine the feasibility of different touchless potential sensing methods. An overview of the cislunar plasma environment is presented in Section II, the effective Debye length theory is outlined in Section III, the methods used to solve for the effective Debye scaling parameters are described in Section IV, the effective Debye length solutions in the solar wind dayside plasma are presented in Section V, the magnetosheath dayside plasma solutions are presented in Section VI, and other factors that may limit servicer–target interactions are investigated in Section VII. The interactions between a servicer and target in cislunar space and the relationship to the effective Debye length are investigated in Section VIII, and the feasibility of passive and active touchless potential sensing is determined in Section IX.

II. CISLUNAR PLASMA ENVIRONMENT

The cislunar plasma environment can be divided into four regions: solar wind, magnetosheath, magnetotail lobes, and plasma sheet, as shown in Fig. 2 [21], [25]. The solar wind region is located outside Earth's magnetic field in the interplanetary magnetic field (IMF) and flowing solar wind. The magnetotail lobes are located inside the magnetopause and mainly consist of plasma outflow from the ionosphere. The plasma sheet is a region of hot plasma located in the center of the magnetotail that magnetically maps to the auroral oval and splits the magnetotail into its top and bottom lobes. It consists of plasma from the solar wind and ionosphere. The magnetosheath is located between the bow shock and magnetopause and is the transition region between the magnetotail lobes and the solar wind. It mainly consists of solar wind plasma that is deflected around the magnetopause [26]. Average characteristic parameters of these regions are shown in Table I [21]. The electron Debye length in the solar wind dayside and magnetosheath dayside regions has the smallest Debye lengths at approximately 10 m, which is considered short for touchless potential sensing, as defined in Section I. Conversely, the electron Debye length is over 100 m in the magnetotail lobes and plasma sheet, which is several times larger than the desired separation distance of 10–30 m for touchless potential sensing. As a result, potential shielding due to the ambient plasma is not a concern in the plasma sheet and magnetotail lobes, and the effective Debye length will be investigated in the solar wind dayside and magnetosheath dayside regions.

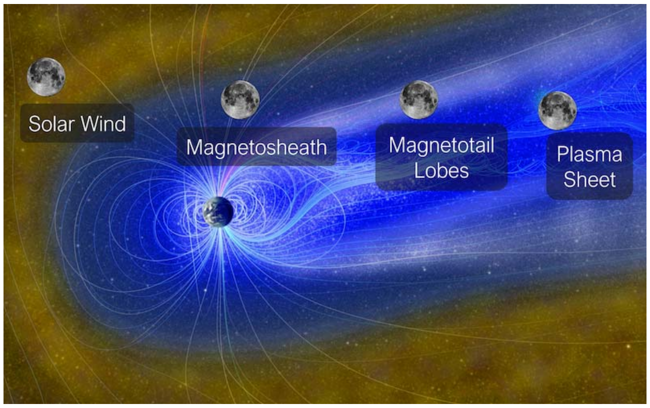

Fig. 2. Cislunar plasma regions.

TABLE I
CISLUNAR REGIONS AVERAGE CHARACTERISTIC PARAMETERS [21]

Region	n_e $(1/m^3)$	T_e (eV)	v_i (km/s)	n_i $(1/m^3)$	T_i (eV)	λ_D (m)
Magnetotail Lobes	2.0E5	48	170	2.0E5	290	115.2
Plasmasheet	2.2E5	150	110	2.0E5	780	194.1
Magnetosheath Dayside	9.5E6	18	350	8.0E6	94	10.2
Solar Wind Dayside	6.0E6	11	420	6.0E6	7	10.1

In addition to orbiting through several regions, when the moon is in the solar wind or magnetosheath region, a lunar wake will develop. The moon removes plasma from the environment through processes such as absorption and reflection. If no other processes occurred, this would leave a void on the anti-sunward side of the moon. However, plasma reenters through various processes, leaving a low-density, complicated plasma structure on the nightside of the moon [27]. As the height above the lunar surface in the wake region increases, the

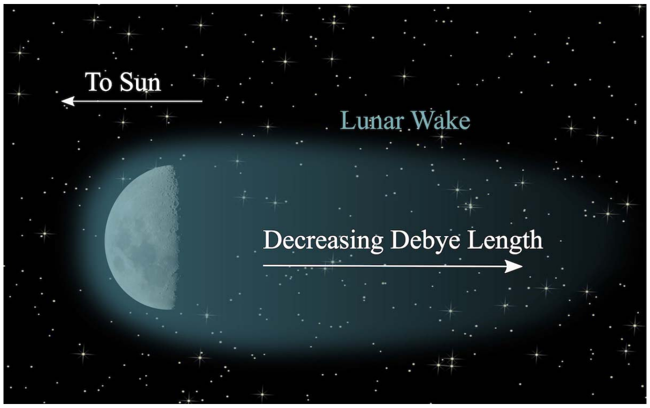

Fig. 3. Lunar wake structure.

plasma returns to the ambient, undisturbed conditions. More specifically, the density of the plasma increases as the height increases. The electron Debye length is found using

$$\lambda_D = \sqrt{\frac{\epsilon_0 k_B T_e}{n_e q_e^2}} \tag{1}$$

where ϵ_0 is the permittivity of free space, k_B is Boltzmann's constant, T_e is the electron temperature, n_e is the electron density, and q_e is the elementary charge. Therefore, as the density increases, the Debye length decreases, as shown in Fig. 3 [21].

III. Effective Debye Length Theory

Several analytic approximations of potential and electric fields in plasma have been developed. The appropriate equations depend on several variables, including the properties of the plasma, potential of the spacecraft with respect to the local plasma, and geometry of the spacecraft [28]. Two models are presented in this research: vacuum (Laplace) and Debye–Hückel. Both assume a spherical spacecraft, and their differing approximations provide a range of potential and electric fields that may be present around a charged sphere in plasma [19], [24].

The vacuum model does not account for space charge shielding or assumes that charge only exists on the spacecraft surface. In a vacuum, the potential field strength at a distance from the center of the sphere is [19]

$$\phi(r) = \frac{V_{SC} R_{SC}}{r} \tag{2}$$

where V_{SC} is the potential of the surface, R_{SC} is the radius of the sphere, and r is the distance from the center. This equation is only valid for $r > R_{SC}$. The electric field is defined as the negative gradient of the potential

$$E(r) = -\nabla_r \phi(r) = \frac{V_{SC} R_{SC}}{r^2}. \tag{3}$$

In a plasma, the potential field is shielded or drops off more rapidly than in a vacuum. The properties of plasma, or the sheath structure, around a charged spacecraft may be determined by solving the Poisson–Vlasov coupled equations using numerical solutions [29]. However, if the charged body is assumed to be a sphere with a low surface potential compared to the plasma thermal energy ($eV_{SC} \ll k_B T_e$), the Debye–Hückel approximation of the potential field can be employed [19]

$$\phi(r) = \frac{V_{SC} R_{SC}}{r} e^{\frac{-(r-R_{SC})}{\lambda_D}}. \tag{4}$$

The electric field is again the negative gradient of the potential field

$$E(r) = -\nabla_r \phi(r) = \frac{V_{SC} R_{SC}}{r^2} e^{\frac{-(r-R_{SC})}{\lambda_D}} \left(1 + \frac{r}{\lambda_D}\right). \tag{5}$$

The potential and electric field as a function of distance from the surface of a spacecraft for a 1-m radius sphere charged to 30 kV in a plasma with a Debye length of 10.1 m is shown in Figs. 4 and 5, respectively. This spacecraft potential is feasible for touchless potential sensing or electrostatic actuation, as electron guns with energies of tens of kilovolts may be utilized, resulting in spacecraft potentials on the order of tens of kilovolts [2], [7], [30]. Note that the electric field is plotted on a log scale, as this allows the features of the models to more easily be compared. The vacuum potential and electric fields are the maximum magnitudes possible, as no potential shielding is taken into consideration. There is an exception within a few meters of the surface of the spacecraft, where the Debye–Hückel model predicts a higher electric field than the vacuum model. In the example plots, the Debye–Hückel model shows a larger electric field within 3.25 m of the surface

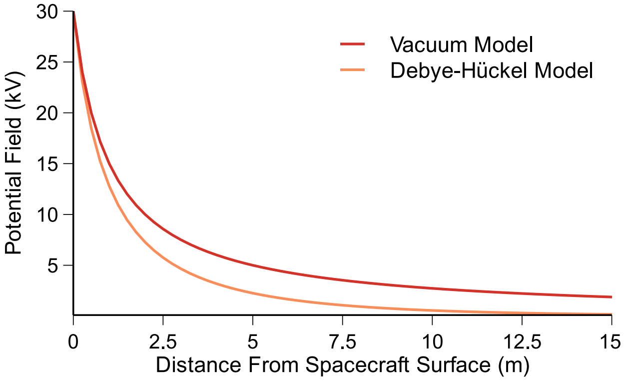

Fig. 4. Potential field for a 30-kV, 1-m radius sphere (λ_D=10.1 m).

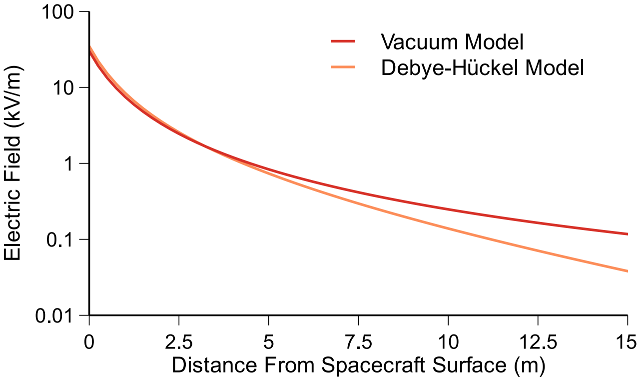

Fig. 5. Electric field for a 30-kV, 1-m radius sphere (λ_D=10.1 m).

of the spacecraft. Therefore, the electric field may be larger than expected close to the spacecraft's surface.

The Debye–Hückel model typically overestimates the potential shielding in a plasma as it assumes that the object's potential is small compared to the energy of the plasma and therefore serves as the minimum estimate of the potential and electric field [24]. Thus, the true fields lie somewhere in between the two models, but the exact location is unknown. As the distance from the surface of the spacecraft increases, the models diverge and uncertainty increases. Furthermore, as the potential of the spacecraft grows with respect to the plasma temperature ($eV_{\text{SC}} > k_B T_e$), the potential field will become closer to the vacuum model. Therefore, developing a more accurate representation of the fields becomes more pressing as the distance from the spacecraft increases and the potential of the surface of the spacecraft increases. This is especially relevant to touchless potential sensing, as it is desirable to have tens of meters of separation between the servicer and the target, and the servicer may be charged to kilovolt levels through the use of an electron gun, as previously mentioned [31], [32].

The Debye–Hückel model may be expanded to represent scenarios in which $eV_{\text{SC}} \not< k_B T_e$. To do so, an effective Debye length is used in place of the electron Debye length [19], [24]. The effective Debye length is simply the Debye length multiplied by a scalar

$$\lambda_{\text{D,eff}} = \alpha \lambda_D. \tag{6}$$

The effective Debye length may be implemented into the Debye–Hückel using the scaling factor α as

$$\phi(r) = \frac{V_{\text{SC}} R_{\text{SC}}}{r} e^{\frac{-(r-R_{\text{SC}})}{\alpha \lambda_D}} \tag{7}$$

and

$$E(r) = \frac{V_{\text{SC}} R_{\text{SC}}}{r^2} e^{\frac{-(r-R_{\text{SC}})}{\alpha \lambda_D}} \left(1 + \frac{r}{\alpha \lambda_D}\right). \tag{8}$$

Finding the effective Debye length is not straightforward. The scaling factor α depends on several variables, including the local plasma parameters, spacecraft surface potential, and spacecraft radius [19], [24]. Therefore, numerical solutions or computational tools must be utilized.

IV. SOLUTION METHODS FOR EFFECTIVE DEBYE LENGTH SCALING FACTOR

In order to compute the effective Debye length scaling factor, the potential field is calculated using numerical or computational tools, and the Debye–Hückel model with the effective Debye length shown in (7) is fit to the solution. The potential field is numerically modeled using the turning point method [19]. The turning point method is based on numerical analysis of possible charged particle orbits in order to solve the Poisson–Vlasov system of equations for spherical geometry [24], [29]. More specifically, the turning point method can be utilized to compute particle density around a charged sphere for a collisionless, isotropic plasma [33]. In this work, the implementation of [29] is used, which provides 1-D electric and potential fields. The turning point method is often considered a nominal solution as it is possible to calculate potential fields over several hundreds of meters with significantly less computational requirements than 3-D plasma analyzers, and the solutions are considered very accurate [29]. This method is also used in [19] and [24] to determine the effective Debye length around asteroids, in a quiet GEO environment, and LEO environments.

In addition to the turning point method, two computational tools are used to determine the scaling parameter: NASCAP-2k and SPIS. NASCAP-2k is a 3-D spacecraft charging and plasma interactions code developed as a collaboration between NASA and the Air Force Research Lab [34], [35]. SPIS is a spacecraft–plasma interaction software created by the Spacecraft Plasma Interactions Network in Europe (SPINE) [36], [37]. Both programs operate with the same basic principles: the object's geometry and computational space are defined, the plasma properties are specified, and methods of evaluation are selected. However, underlying processes and assumption of the programs vary. Therefore, utilizing both tools allows for a better understanding of the range of α terms that may be applicable for a charged spacecraft in a plasma environment. Furthermore, the use of 3-D computational tools to calculate the scaling parameter allows for an investigation into the accuracy and functionality of these programs for large computational volumes. Once the potential field is found in the programs, the α term is found using a nonlinear least squares fit to the entire potential field solution. The accuracy of the fit is investigated in Section V.

To define computation in NASCAP-2k, several parameters must be defined. First, the spacecraft is defined in the *Object Toolkit*. For this research, a spherical shape is approximated in order to properly compare the results to the turning point method. Next, the computational space is defined using a Cartesian grid. More specifically, a parent grid is defined that encompasses the computational space, and child grids are defined where better resolution is desired. Typically, child grid elements are a factor of 2 smaller than their parent grid elements. Next, the interplanetary environment is selected with 100% H^+ ions [17], [34]. To calculate the potentials in space, the analytic nonlinear model is selected, as it is applicable to high and low potentials in a dense plasma and is appropriate when the spacecraft velocity and the ambient magnetic field have minimal effect on the charge density within the sheath. This function interpolates between linear Debye screening (the Debye–Hückel model) at low potentials and the charge density of a single accelerated and converging species at high potentials to solve Poisson's equation [28], [38]. To do so, the model uses a convergence factor, which accounts for increased charge density due to attracted charged particles. The convergence factor was determined by numerically solving the Langmuir and Blodgett problem for current collection by a biased sphere [39] and fitting an analytic formula to the results [34]. While the plasma densities in cislunar space, shown in Table I, are low compared to LEO plasma, strict limits are not placed on the density for the nonlinear model and high-density plasma is interpreted to apply to environments in which the Laplace, or vacuum, model is not applicable. Other model options for the interplanetary space environment include

TABLE II

NASCAP-2K PARENT GRID SIZING FOR A 30-kV, 2-m RADIUS SPHERE

Distance from sphere center to external boundary (m)	α	**Percent Difference (%)**
14	1.949	NA
28	3.007	42.70
56	4.787	45.68
112	7.047	38.20
224	7.279	3.24

TABLE III

NASCAP-2K GRID RESOLUTION SIZING AROUND A 30-kV, 0.25-m RADIUS SPHERE

Element size around sphere (m)	α	**Percent Difference (%)**
2	4.447	NA
1	1.850	82.48
0.5	2.496	29.73
0.25	2.495	0.04

TABLE IV

SPIS EXTERNAL BOUNDARY SIZING FOR A 30-kV, 2-m RADIUS SPHERE

Distance from sphere center to external boundary (m)	α	**Percent Difference (%)**
70	4.326	NA
90	5.156	17.51
110	6	15.13
130	5.648	6.04

TABLE V

SPIS EXTERNAL BOUNDARY GRID SIZING FOR A 30-kV, 0.25 m RADIUS SPHERE

Boundary element size (m)	α	**Percent Difference (%)**
30	1.619	NA
20	1.874	14.60
10	1.956	4.28

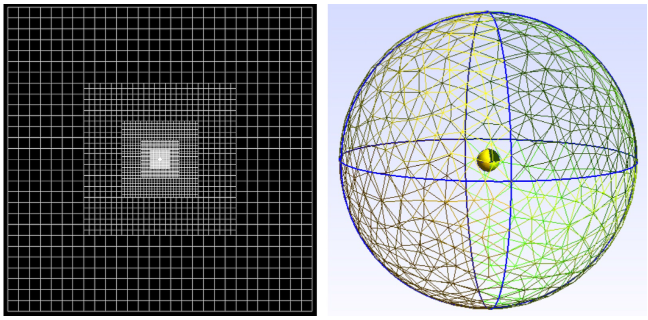

Fig. 6. NASCAP-2k cut view of grid (left) and SPIS 2-D mesh (right).

barometric and full trajectory ion, which are applicable when current collection in a wake is important, and frozen ion, which is intended for primarily for negative potentials [35]. As a result, the nonlinear model is the most appropriate assumption. The boundary conditions for the grid is set to "DEBYE," which estimates the potential on the boundary of the grid using the Debye–Hückel approximation. It should be noted that cislunar spacecraft may have a nonnegligible velocity with respect to the plasma, but this is not considered in this study.

In order to ensure that the results are independent of the grid, analysis is conducted to determine the optimal size and resolution of the grids. First, the size of the parent grid is determined by increasing the size of the external boundary until the difference in solution is below 10%. This analysis is conducted for a 30-kV, 2-m radius sphere, as this is the most extreme case to be analyzed. The results are shown in Table II. Once the external boundary is set, the resolution required around the spacecraft is increased by adding child grids with a subdivision ratio of 2 until the difference in solution is once again below 10%. This is conducted for a 30-kV, 0.25-m radius sphere, as this is the smallest spacecraft to be investigated and will require the highest resolution near the surface. The resolution results are shown in Table III. A cut view of the final NASCAP-2k grid is shown in Fig. 6.

SPIS also requires that several parameters are defined in order to perform a computation. The geometrical system is first defined, which must include the external boundary, the inner boundary (spacecraft surface), and the computational volume bound by the external and inner boundaries. Once the computational space is defined by the geometry, it is meshed with irregular tetrahedral elements, which is built and optimized in Gmsh, a 3-D finite-element mesh generator [37]. Once the mesh is built, the Dirichlet boundary condition is selected, which assumes a fixed boundary potential. The potential is then set equal to the potential estimated at that distance by the Debye–Hückel model. In addition, the external boundary is defined using a sphere so that the entire surface is equidistant from the spherical spacecraft surface. To model the ions and electrons, SPIS offers a Maxwell–Boltzmann and particle-in-cell (PIC) distribution. For this study, the PIC distribution is selected for both ions (100% H^+) and electrons, as a Maxwell–Boltzmann distribution assumes that the potential of the spacecraft is significantly less than the energy of the plasma. The PIC method conducts Monte Carlo solving of the Vlasov equation using ion and electron macroparticles.

The SPIS mesh is also analyzed to ensure the results independent of the mesh. The size of the external boundary is increased until the difference in solution is less than 10%, and the spacecraft is again defined as a 30-kV, 2-m radius sphere. The analysis and external size results are shown in Table IV. Once the external boundary is determined, an intermediate grid with a 0.5-m resolution and 8-m radius is added to slow the size of the mesh expansion near the spacecraft. Then, the resolution of the external mesh is increased until the difference is less than 10% for a 30-kV, 0.25-m radius sphere, as shown in Table V. The final 2-D mesh is shown in Fig. 6.

V. DAYSIDE SOLAR WIND EFFECTIVE DEBYE LENGTHS

The effective Debye lengths in the dayside solar wind region are investigated as this region has the shortest electron Debye length, and the moon spends approximately two thirds of its orbit in the solar wind [40]. The parameters in Table I are used for this analysis. As shown, the electron temperature is only 11 eV, so if the potential of the surface of the spacecraft is only a few volts, the potential of the spacecraft

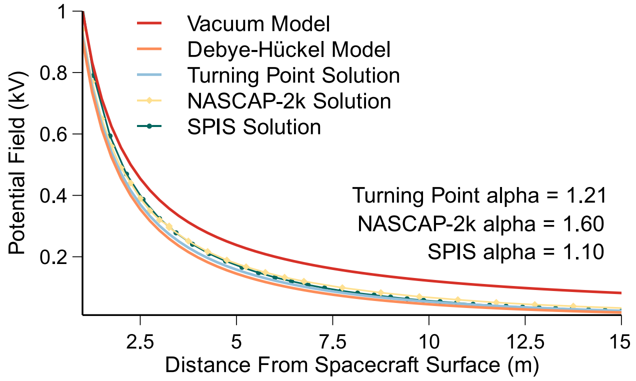

Fig. 7. Potential field models for a 5-kV, 0.25-m radius sphere in mean solar wind dayside plasma.

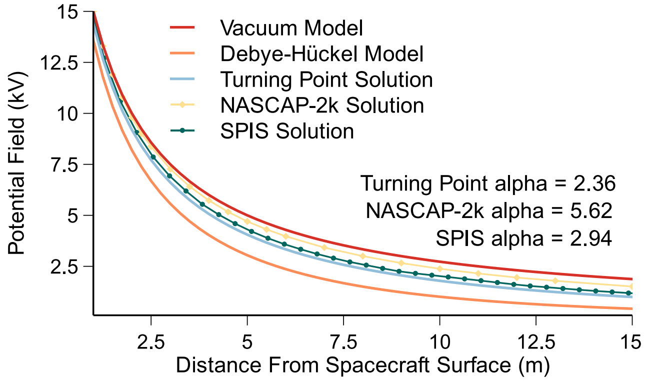

Fig. 8. Potential field models for a 30-kV, 1-m radius sphere in mean solar wind dayside plasma.

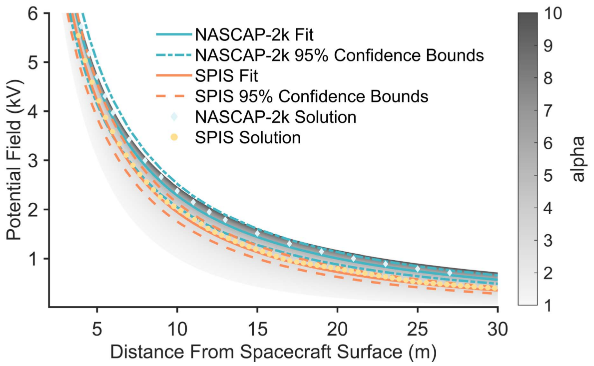

Fig. 9. SPIS and NASCAP-2k solutions, fits, and confidence bounds for a 30-kV, 1-m radius sphere in mean solar wind dayside plasma. A background grayscale colormap shows the potential field versus distance for a range of α.

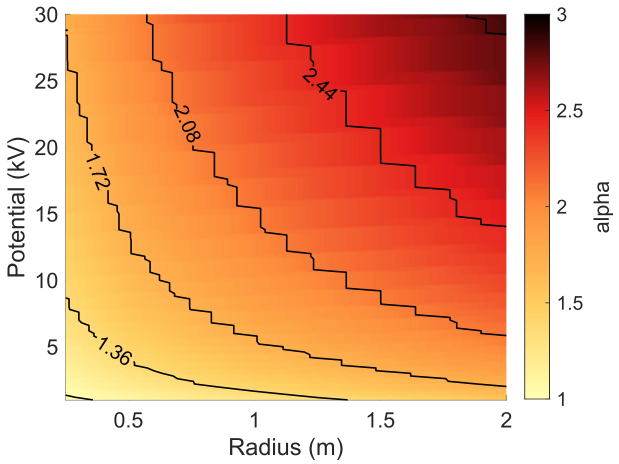

Fig. 10. Trends in effective Debye length scaling factor α in the dayside solar wind region computed using the turning point method.

surface is not significantly less than the plasma thermal energy ($eV_{\mathrm{SC}} \not< k_B T_e$). Example potential field computations are shown in Figs. 7 and 8. As shown, as the radius and potential of the spacecraft increase, the effective Debye length increases. This follows expectations, as the potential field is expected to approach the vacuum model as the potential of the spacecraft increases. The scaling factor results for each model differ slightly, as expected, but the potential fields versus distance results are comparable. Furthermore, all models lie in between the Debye–Hückel and vacuum potential fields, and they display the same trend as the radius and potential increases.

The NASCAP-2k and SPIS solutions, fits, and confidence bounds for a 30-kV, 1-m radius sphere are shown in Fig. 9. In the background of the plot, the potential field versus distance is shown as a grayscale colormap for different scaling parameter values for comparison. Interestingly, the potential field seems to change more significantly when the alpha parameter is smaller. For example, at a distance of 15 m from the spacecraft surface, the difference in potential field magnitude calculated for alpha values of 1 and 1 is approximately 500 V, while the potential field magnitude difference between alpha values of nine and ten is approximately 27 V. This explains why the scaling parameters vary significantly between models despite similar potential field versus distance results. The scaling parameter value is more uncertain as spacecraft potential and radius increases, but this does not necessarily correspond to higher uncertainty in the potential field approximation. Therefore, the potential field may still be approximated by the range of scaling parameters found using the three previously described methods.

In order to evaluate the effective Debye length scaling factor trends, computations are done for radii ranging from 0.25 to 2 m and potentials ranging from 1 to 30 kV. The solutions found using the turning point method are shown in Fig. 10. As shown, a higher spacecraft radius and potential result in a higher α, with a maximum scaling factor at 2.85. There are physical limits on the potential and radius that a cislunar craft may achieve, but this solidifies that the effective Debye length may be increased in the dayside solar wind.

The NASCAP-2k, SPIS, and turning point scaling parameter solutions are compared, as shown in Fig. 11. NASCAP-2k and SPIS solutions typically overestimate the alpha parameter, or underestimate the potential shielding, compared to the turning point method. Furthermore, the NASCAP-2k solutions appear to show the same trend seen in the turning solutions, as the rate at which alpha is changing decreases consistently as the potential increases. The SPIS solutions by contrast appear to increase more sporadically, but the magnitude of the scaling parameters is closer to the turning point solutions. The

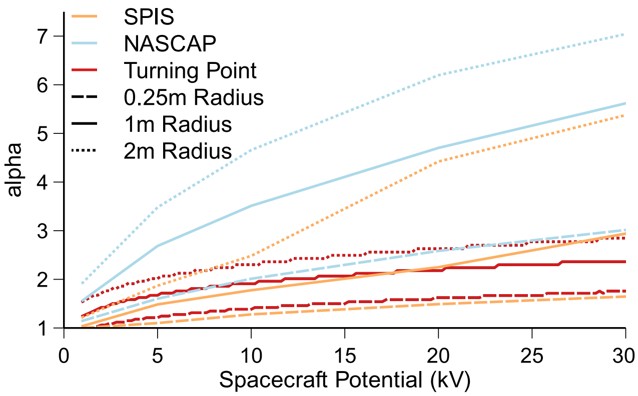

Fig. 11. NASCAP-2k, SPIS, and turning point α solutions versus spacecraft potential for spheres with varying radii.

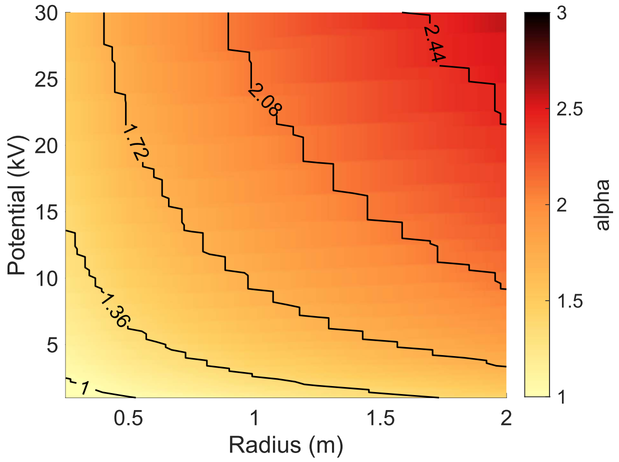

Fig. 12. Trends in the effective Debye length scaling factor α in the dayside magnetosheath region computed using the turning point method.

differences in solutions may be explained by the mesh analysis and difference in the solution method, described in Section IV, and the uncertainty of the model fit to the solutions. In addition, the numerical accuracy limits of NASCAP-2k and SPIS may be pushed as the potential field is computed over the large computational volume. Anyway, the use of all three methods presents a narrow range of solutions that may be used to predict the potential fields expected in solar wind dayside plasma. Furthermore, despite the differences in magnitude, all methods show that as the radius and potential increase, the scaling parameter increases. This is promising for touchless potential sensing, as it may be possible at larger separation distances than expected.

VI. DAYSIDE MAGNETOSHEATH EFFECTIVE DEBYE LENGTHS

The scaling parameter trends are also evaluated using the turning point method in the dayside magnetosheath region as the electron Debye length is only 10.2 m, and the electron temperature is again low at 18 eV, as shown in Table I. The scaling parameter results found using the turning point method are shown in Fig. 12. The trends are similar to the solar wind scaling parameter trends, as α increases nonlinearly with increasing potential and radius. However, the scaling parameter values are smaller, with a maximum α at approximately 2.59. This is likely due to the higher electron temperature and electron Debye length. Nevertheless, this shows that increasing the potential and radius of the servicer can increase the effective Debye length and enable touchless potential sensing at farther distances in the dayside magnetosheath region as well.

VII. CONSIDERATION OF OTHER LIMITING FACTORS

In order to touchlessly sense the potential of a neighboring target spacecraft, the servicer is charged more positively than the target such that the emitted electrons are attracted toward the servicer. However, if the target's emitted electrons cannot "see" the servicer or the servicer's potential field does not extend to the target, the emitted electrons may not be attracted to the servicer. Some emissions may still reach the servicer if their trajectory happens to intercept the servicer, but in this scenario, the measured current is limited and may not be detectable. Therefore, the optimal separation distance is theorized to be within the sum of the effective Debye lengths of the servicer and target. However, other factors that may deflect emissions must be considered, including the magnetic field and particle collisions. The gyroradius or the radius of the circular motion of a nonrelativistic charged particle in a magnetic field is

$$r_g = \frac{v_\perp m_e}{q_e B} \tag{9}$$

where $v_\perp$ is the velocity perpendicular to the magnetic field, m_e is the mass of an electron in kilograms, and B is the magnetic field strength in teslas. The thermal velocity of an electron is

$$v_e = \sqrt{\frac{2k_B T_e}{m_e}}. \tag{10}$$

In the ambient solar wind at 1 AU, the IMF is approximately 4 nT [41]. The magnetic field in the magnetosheath is complex, and extensive studies have been conducted to parameterize it [42]. In general, the IMF may be amplified in the magnetosheath, and the magnetic field is estimated as 10 nT based off data from Cluster 1 [43], [44].

Using the parameters from Table I and assuming that the electron velocity is entirely perpendicular to the magnetic field, the gyroradius of electrons is approximately 2.8 km in the dayside solar wind and 1.4 km in the dayside magnetosheath plasma. Separation distances of tens of meters are proposed for touchless potential sensing, which is significantly less than the gyroradius. Therefore, deflection from the servicer due to the magnetic field does not limit sensing capabilities.

The distance at which particles travel between collisions is characterized by the mean free path, λ_{mfp}. The mean free path of particles in a Maxwellian plasma is [45]

$$\lambda_{\text{mfp}} = \frac{48\sqrt{6/\pi}\, N_D \lambda_D}{\ln(9N_D)} \tag{11}$$

where N_D is the Debye number or the number of particles in a sphere with radius equal to the Debye length

$$N_D = \frac{4}{3}\pi n_e \lambda_D^3. \tag{12}$$

The mean free path is approximately 6.5E8 km in dayside solar wind and 10.8E8 km in dayside magnetosheath plasma, which is orders of magnitude larger than the proposed touchless potential sensing scale. Therefore, collisions are also not a limitation for sensing in these regions.

VIII. SERVICER–TARGET INTERACTIONS

In order to investigate the influence of effective Debye lengths on particle motion, two aluminum, 1-m radius spherical spacecraft, a servicer and target, are modeled in dayside solar wind plasma in NASCAP-2k. As found in Section V, NASCAP-2k overestimates the scaling parameter when compared to the turning point solutions. However, the scaling parameter trends better follow the trends found using the turning point method, as the scaling parameter increases with increasing radius and potential and the rate of change decreases with increasing potential. The purpose of this section is to analyze trends in servicer–target interactions, so the magnitude of the sheath is of secondary importance compared to the trends in sheath size. In addition, the difference in the potential field versus distance from the spacecraft surface is shown to be small for the larger scaling parameter solutions in Section V, so the NASCAP-2k potential field estimates are a reasonable approximation. Therefore, the findings in NASCAP-2k are analyzed as an approximation and show the general interactions between a servicer and target in the cislunar solar wind. The conclusions drawn from the simulations also apply to the dayside magnetosheath environment, as the effective Debye length is on a similar scale and the other factors investigated were also not found to be a concern in this region.

The servicer is held to 1 and 10 kV in order to determine the impact of different effective Debye lengths and potential magnitudes on servicer–target interactions; 1 kV is chosen as the lower bound, as this is the lowest potential at which the effective Debye length has been investigated; 10 kV is chosen for comparison as this is a reasonable potential for touchless potential sensing and the electrostatic tractor, and it allows for comparison between servicers with an order of magnitude difference in potential. The target is allowed to float in order to analyze how different servicer potentials and separation distances may impact the target's potential and electron emissions. The target is simulated at distances of 10, 20, 40, and 100 m in order to analyze how the interactions change with changing separation distances. The grid definition is based on the findings from Section IV. Thus, the external boundary is defined at least 100 m from the edge of both spacecraft, and the grid elements are smaller than 0.5 m near the surface of the spacecraft. Fig. 13 shows the grid for a distance of 10 m between the servicer and the target.

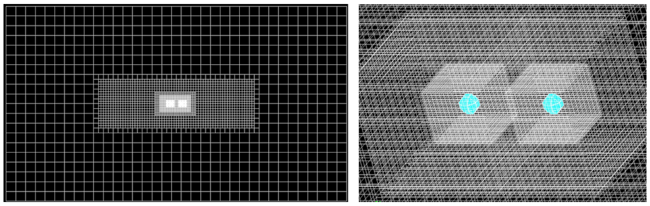

Fig. 13. Cutaway of NASCAP-2k grid for computation with 10-m separation between spacecraft (left) and resolution of the grid around spacecraft surfaces (right).

The NASCAP-2k analysis requires two steps to investigate the servicer and target interactions: computation of target charging and potentials in space, and simulation of emitted particle trajectories. For the first step, the surface charging is computed using the "Tracked Ion & Analytic Electron Currents" option. For this option, the electron surface currents are calculated using analytic formulas appropriate for the specified environment, interplanetary Maxwellian plasma for this case. The ion surface currents are taken from particle tracking results, and for this study, the ion particles are generated as a thermal distribution at the grid boundary. The potentials in space are once again found using the analytic nonlinear option. Once the potentials in space and target potential are found, the emitted particle trajectories are simulated. NASCAP-2k does not automatically provide an option to simulate emitted particle trajectories. However, spacecraft surfaces may be assigned as "Emitters" in the *Object Toolkit*. For an emitter, the emitted current density, range of angles, and range of kinetic energies are specified, and the particles may then be tracked from the surface. After computing the floating potential of the target, various current densities can be found on the "Results" tab. For an eclipse environment, which may occur if the target is shadowed by the servicer or other spacecraft, the secondary electron current is the dominant emitted current. The angular distribution of secondary electrons approximately follows a Lambertian distribution and is nearly independent of the impacting particle's angle of incidence [6], [46]. Therefore, the range of angles is defined as zero to π or the highest range of emitted angles possible. The emitted energy of a secondary electron is on the order of a few electronvolts and follows a characteristic distribution, often modeled using the Chung–Everhart probability density function, with a peak at one third of the work function φ of the material [47]. The work function of aluminum is assumed to be 4 eV [48], so the energy of the secondary electrons is defined as 1.333 eV. Once the emitter is defined, the trajectories are modeled as particles injected into the computational space from the surface of the spacecraft.

The dayside solar wind environment is, as the name implies, a sunlit environment. Therefore, computations are also conducted in sunlight, and in sunlight, the photoemission current exceeds other current contributions. The photoemission current density can again be found in the "Results" tab. Since photoelectrons are a case of secondary electrons emitted by photons as opposed to incident electrons, the angular distribution again follows a Lambertian distribution, and the range of angles is defined from zero to π. The maximum emission energy follows the relation:

$$E_{\text{ph,max}} = \omega - \varphi \tag{13}$$

TABLE VI
POTENTIAL AND CURRENT DENSITY OF ELECTRON EMISSIONS FOR A 1-m RADIUS TARGET NEAR A 10-kV, 1-m RADIUS SERVICER

Separation distance (m)	**Target potential in eclipse (V)**	**SEE current density $(\mathrm{A/m^2})$**	**Target potential in sunlight (V)**	**Photoelectron current density $(\mathrm{A/m^2})$**
10	-179.3	7.838E-15	5.021	3.249E-6
20	-128.2	8.157E-13	5.021	3.249E-6
40	-123.4	1.260E-12	5.021	3.249E-6
100	-24.18	1.046E-8	5.021	3.249E-6

where ω is the incident photon energy and φ is the work function. The Ly–α line is the dominant wavelength in the solar spectrum at 10.2 eV, so in theory, photoelectrons will be generated from aluminum surfaces at approximately 6.2 eV. However, photoelectrons must be excited in a direction such that it can propagate through the material and overcome the work function barrier. Following this process, photoelectrons emerge from the surface with typical energies between 1 and 3 eV [32], [49]. Therefore, the emitted energy is set from 1 to 3 eV. In addition, photoelectrons are only emitted from half the target, as only half of the sphere will be sunlit.

A. 10-kV Servicer Results

The results are presented for the 10-kV servicer. The effective Debye length for this servicer as found in NASCAP-2k is 35.1 m, so the approximate distance at which the servicer is theorized to be capable of attracting the target's emissions is 45.2 m, the sum of the servicer's effective Debye length and the electron Debye length. The target's resulting potentials and currents in eclipse and sunlight are shown in Table VI. In eclipse, as the target moves closer to the servicer, the surface potential becomes more negative. This may be contributed to a change in charging currents because the positive servicer repels ions and attracts electrons, so as the target moves closer to the servicer, the flux of incident electrons increases and incident ions decreases. In addition, the presence of a charged neighboring object alters the capacitance of a spacecraft as a function of the separation distance, which in turn alters the spacecraft potential [50]. In addition, the secondary electron current density decreases as the target approaches the servicer. Ambient electrons are accelerated to the energy of the servicer as they approach it, and secondary electron emissions favor lower energy incident electrons [51]. More specifically, $E_{\max}$ of aluminum, or the energy corresponding to the maximum secondary electron yield, is 300 eV, significantly less than the potential of the servicer [48]. Furthermore, there is a larger change in potential closer between 10 and 20 m than between 20 and 40 m. This is expected, as the potential field changes at a higher rate closer to a charged spacecraft, as shown by the potential fields in Figs. 4, 7, and 8. In sunlight, the photoemission current exceeds other contributing currents, so the target potential remains at a positive 5.021 V for all positions.

The secondary electron emissions modeled are shown in Fig. 14. The secondary electron trajectories are tracked throughout the grid but are only shown in a section of the grid in order to more clearly visualize individual trajectories. As a result, some trajectories appear to stop suddenly, but these simply left the bounds of what is plotted. As expected, regardless of separation distance, the secondary electron emissions are accelerated away from the negative target, and once the electrons are within the sphere of influence of the servicer, their trajectories are warped toward the servicer and may impact the surface. This is promising for touchless potential sensing, as emissions may reach the servicer at distances far exceeding the effective Debye length. However, at larger separation distances, fewer emissions are drawn toward the servicer, and the detected currently likely decreases. This will be explored further in Section IX.

The photoelectron trajectories from a sunlit target are shown in Fig. 15. Since the target charges positively in sunlight, the photoelectrons are not repelled from the target spacecraft and in isolation would be attracted back toward the target. However, if the potential field of the positive servicer exceeds that of the target, seen at separation distances of 10–40 m, the photoelectrons emitted from all sides of the target are drawn toward the servicer. These emissions then impact the servicer or enter complex trajectories that appear to orbit the servicer and target. This may lead to more positive potentials on the target, but this effect is not accounted for in NASCAP-2k computations and may be a subject of future work. At 100 m of separation, the servicer and the target do not interact with each other, as they are farther than approximately 45.2 m apart. As a result, the low-energy photoemissions are attracted back toward the positively charged target and are not detected by the servicer.

B. 1-kV Servicer Results

The results are presented for the 1-kV servicer. The effective Debye length found for this servicer in NASCAP-2k is approximately 15.8 m. Thus, the servicer is theorized to be capable of attracting the target's emissions within a separation distance of 25.9 m, the sum of the servicer's effective Debye length and the electron Debye length. The target's resulting potentials and currents in eclipse and sunlight are shown in Table VII. The same trends are seen as in the previous section, as the target becomes more negative and the secondary electron current decreases as it approaches the servicer. However, the target potential is more positive and the secondary electron current is larger in comparison. This makes sense, as the 1-kV servicer does not attract as many electrons and repel as many ions as the 10-kV servicer. Furthermore, the electrons are not accelerated as much as they approach the servicer, so their energy remains closer to the $E_{\max}$ energy of 300 eV. In addition, the potential approaches its isolated, floating potential at smaller separation distances than the previous case. This is expected,

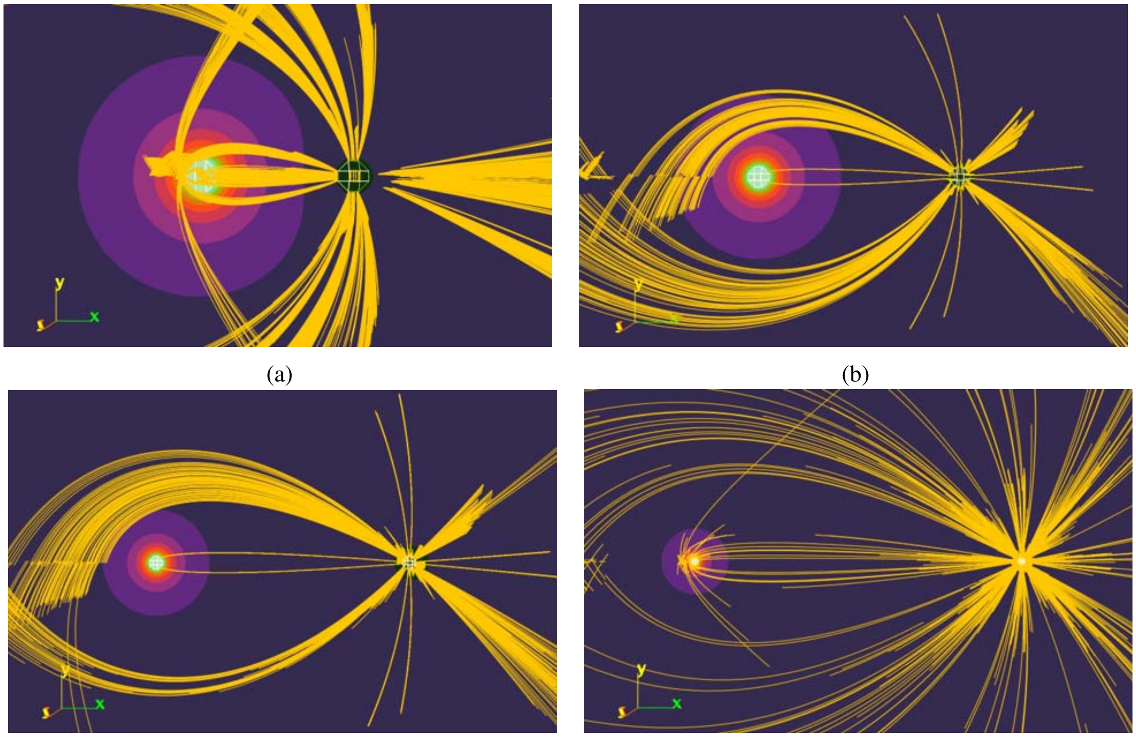

(a) (b) (c) (d)

Fig. 14. Secondary electron trajectories from a negatively charged 1-m radius target (right) in eclipse at varying distances from a 10-kV, 1-m radius servicer (left). (a) 10-m separation, $V_{\text{fl,target}}$. (b) 20-m separation, $V_{\text{fl,target}}$. (c) 40-m separation, $V_{\text{fl,target}}$. (d) 100-m separation, $V_{\text{fl},target}$.

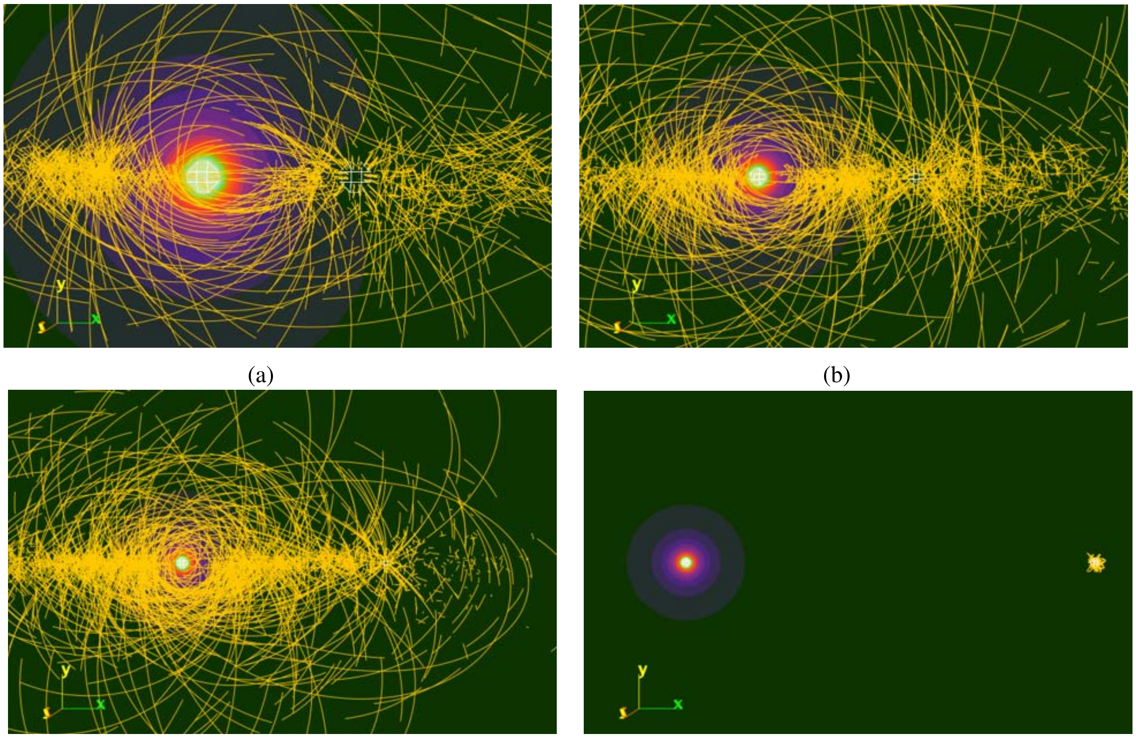

(a) (b) (c) (d)

Fig. 15. Photoelectron trajectories from a 5.021-V, 1-m radius target (right in sunlight at varying distances from a 10-kV, 1-m radius servicer (left). (a) 10-m separation. (b) 20-m separation. (c) 40-m separation. (d) 100-m separation.

as the effective Debye length for a 1-kV servicer is shorter than that for a 10-kV servicer. Thus, the potential field and the servicer interactions with the target will decrease more rapidly. The potential in sunlight is once again dominated by

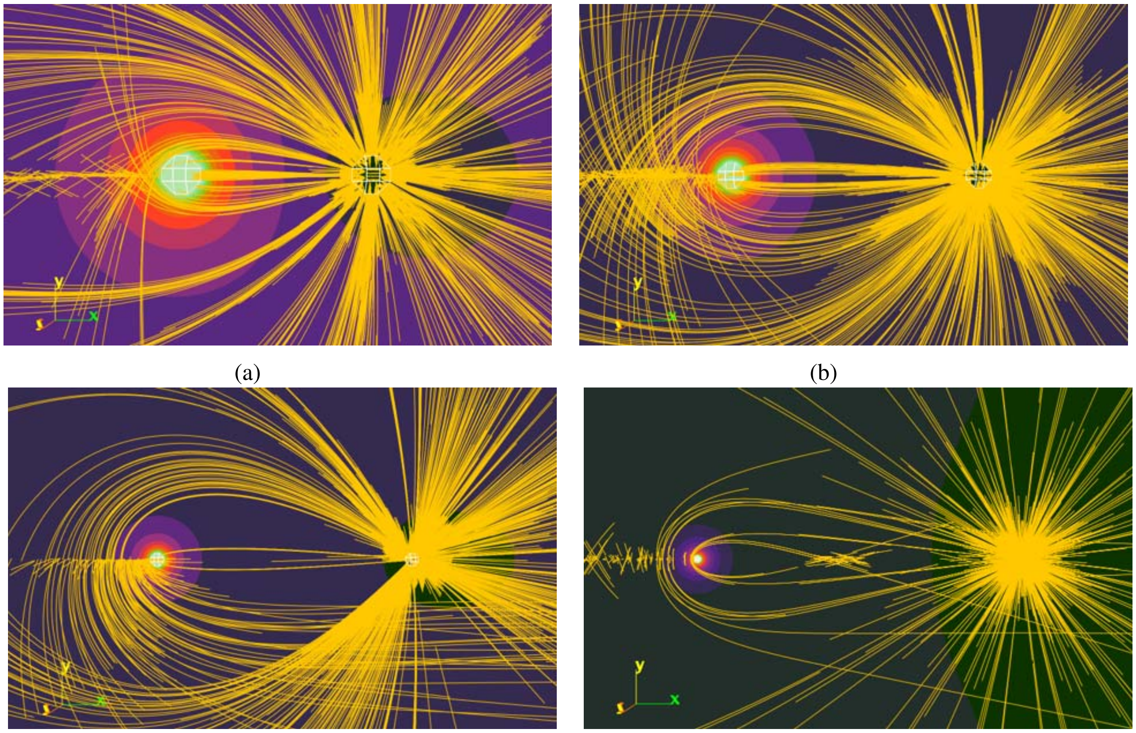

(a) (b)

(c) (d)

Fig. 16. Secondary electron trajectories from a negatively charged 1-m radius target (right) in eclipse at varying distances from a 1-kV, 1-m radius servicer (left). (a) 10-m separation, $V_{\text{fl,target}}$. (b) 20-m separation, $V_{\text{fl,target}}$. (c) 40-m separation, $V_{\text{fl,target}}$. (d) 100-m separation, $V_{\text{fl,target}}$.

the photoemission current, and the target potential is the same as the previous case and remains unchanged as the servicer approaches the target.

The modeled secondary electron emissions are shown in Fig. 16. Again, the trajectories are modeled through the entirety of the grid, but only a section of the trajectories are shown in order to more easily evaluate individual trajectories. The same behavior is seen as the previous case, as secondary electrons are accelerated away from the negative target and may enter the potential field of the servicer. However, the potential field, or sheath size, of the 1-kV servicer is smaller than that of the 10-kV servicer, so less emission trajectories are influenced by the potential field of the servicer.

The photoelectron trajectories are shown in Fig. 17. The emissions are attracted to the servicer from all sides at separation distances of 10 and 20 m and again either impact the servicer or enter into complex trajectories. At 40 m of separation, the servicer and target are approximately 14 m farther apart than their combined Debye lengths. However, some of the trajectories from the near side of the target are still attracted toward this servicer. Upon further investigation, it is found that the potential field surrounding the servicer is 3 V, or the maximum energy of the photoelectrons, near the closest side of the target, as shown in Fig. 18. Therefore, the most energetic photoemissions emitted from the side of the target nearest the servicer reach the point at which the potential field of the servicer exceeds the potential field of the target and are pulled directly toward the servicer. At 100-m separation, the servicer and target once again do not interact with each other, so the photoemissions are attracted back toward the target.

C. Comparison to Vacuum and Debye–Hückel Model

In order to verify the importance of using the effective Debye length to calculate potential fields instead of the electron Debye length or the vacuum model, the photoelectron trajectories are modeled in NASCAP-2k using the “Laplace” and “linear (Debye shielding)” potentials in space options. The Laplace, or vacuum, model assumes zero space charge, or the charge exists only on the object surfaces, as approximated by (2) and (3). This is the approximation that has been utilized in investigations in the GEO environment. The linear (Debye shielding) model solves the Debye–Hückel equation using the electron Debye length, as shown in (4) and (5). Therefore, these options provide a method to compare the servicer–target interactions found using the effective Debye length to the models outlined in Section IV. The target potential and photoelectron current density are kept the same as in Table VII in order to allow for direct comparison.

The trajectories found using the listed models are shown in Fig. 19. The photoelectron trajectories modeled using the Laplace model more closely resemble the results in Fig. 16 when the target is negatively charged. In other words, the Laplace assumption overestimates the servicer’s potential field, so photoemissions are attracted at distances far exceeding the combined effective Debye lengths. Thus, this model does not accurately capture the potential field damping that occurs in the plasma environment and vastly overestimates the distance at which the servicer can sense the target’s potential. At 40 m, the servicer and target are no longer interacting in the Debye–Hückel model, which shows an overestimation of the potential

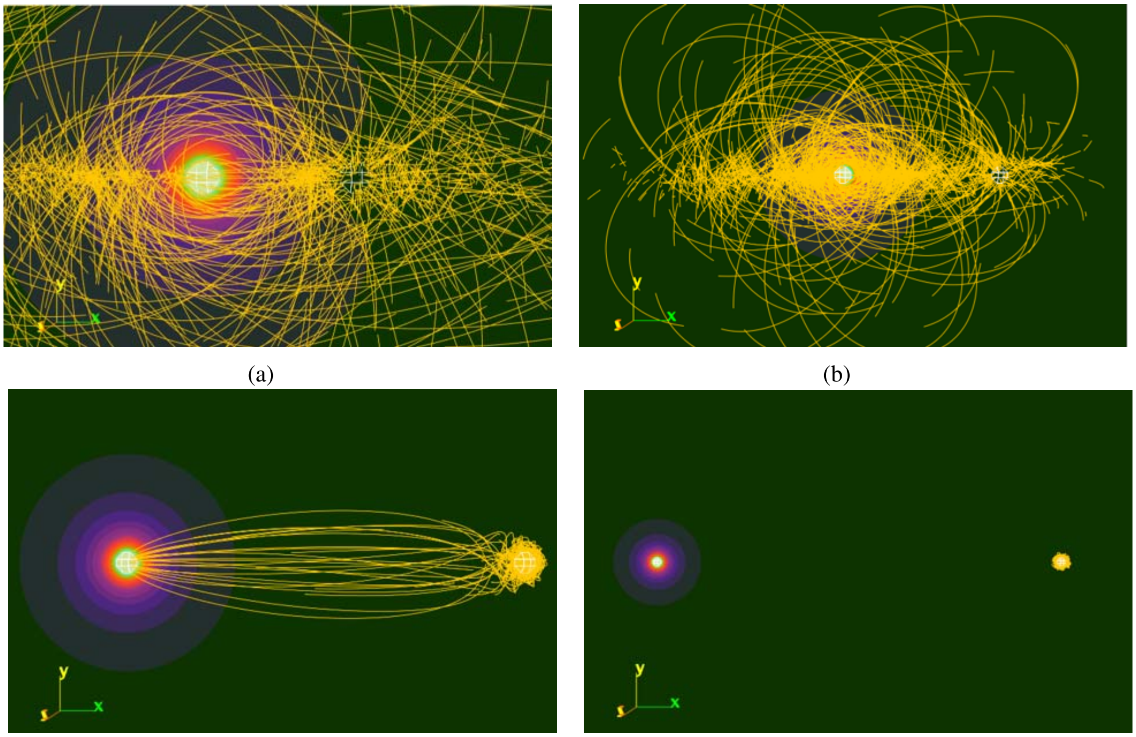

(a) (b)

(c) (d)

Fig. 17. Photoelectron trajectories from a 5.021-V, 1-m radius target (right) in sunlight at varying distances from a 1-kV, 1-m radius servicer (left). (a) 10-m separation. (b) 20-m separation. (c) 40-m separation. (d) 100-m separation.

TABLE VII

POTENTIAL AND CURRENT DENSITY OF ELECTRON EMISSIONS FOR A 1-m RADIUS TARGET NEAR A 1-kV, 1-m RADIUS SERVICER

Separation distance (m)	**Target potential in eclipse (V)**	**SEE current density $(\mathbf{A/m^2})$**	**Target potential in sunlight (V)**	**Photoelectron current density $(\mathbf{A/m^2})$**
10	-162.7	3.563E-14	5.021	3.249E-6
20	-29.86	7.536E-9	5.021	3.249E-6
40	-12.16	3.121E-8	5.021	3.249E-6
100	-11.89	3.196E-8	5.021	3.249E-6

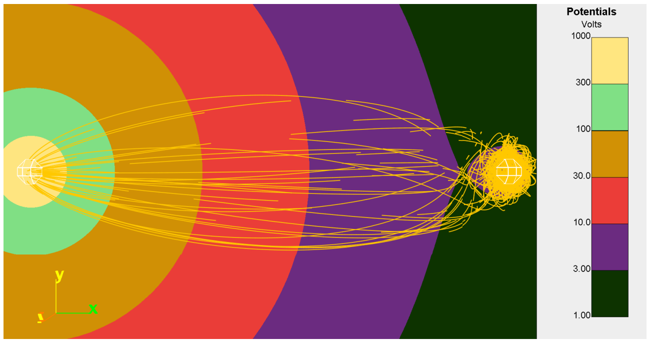

Fig. 18. Potential field and photoemission trajectories for a 1-kV, 1-m radius servicer (left) and 5.021-V, 1-m radius target (right) at a separation distance of 40 m.

field damping compared to the previous section. Therefore, the distance at which the servicer can sense the target's potential is underestimated using this model. As found in the previous section, the effective Debye length is already a conservative estimate for the distance at which the servicer can detect the target's emissions, so the Debye–Hückel model is not useful for estimating possible potential sensing distances. In addition, the use of the Laplace or Debye–Hückel model may overestimate and underestimate, respectively, the Coulomb force between the target and servicer and the current detected by the servicer due to the models' inaccuracies when determining the servicer's potential field.

IX. TOUCHLESS POTENTIAL SENSING

Now that the possible separation distance between a servicer and a target for electron emissions from the target to be capable of reaching the servicer has been investigated, the feasibility of touchless potential sensing is determined. In order to touchlessly sense the potential of a target without the use of an electron beam or UV laser, the natural emissions from the target must be distinguishable from the ambient plasma environment. In other words, within the maximum separation distance at which interactions occur, discussed in Sections VIII-A and VIII-B, sufficient current must reach the servicer's sensor. Electrostatic analyzers (ESAs) are used to measure the ambient charged particle distribution function [52]. For this work, a retarding potential analyzer (RPA)

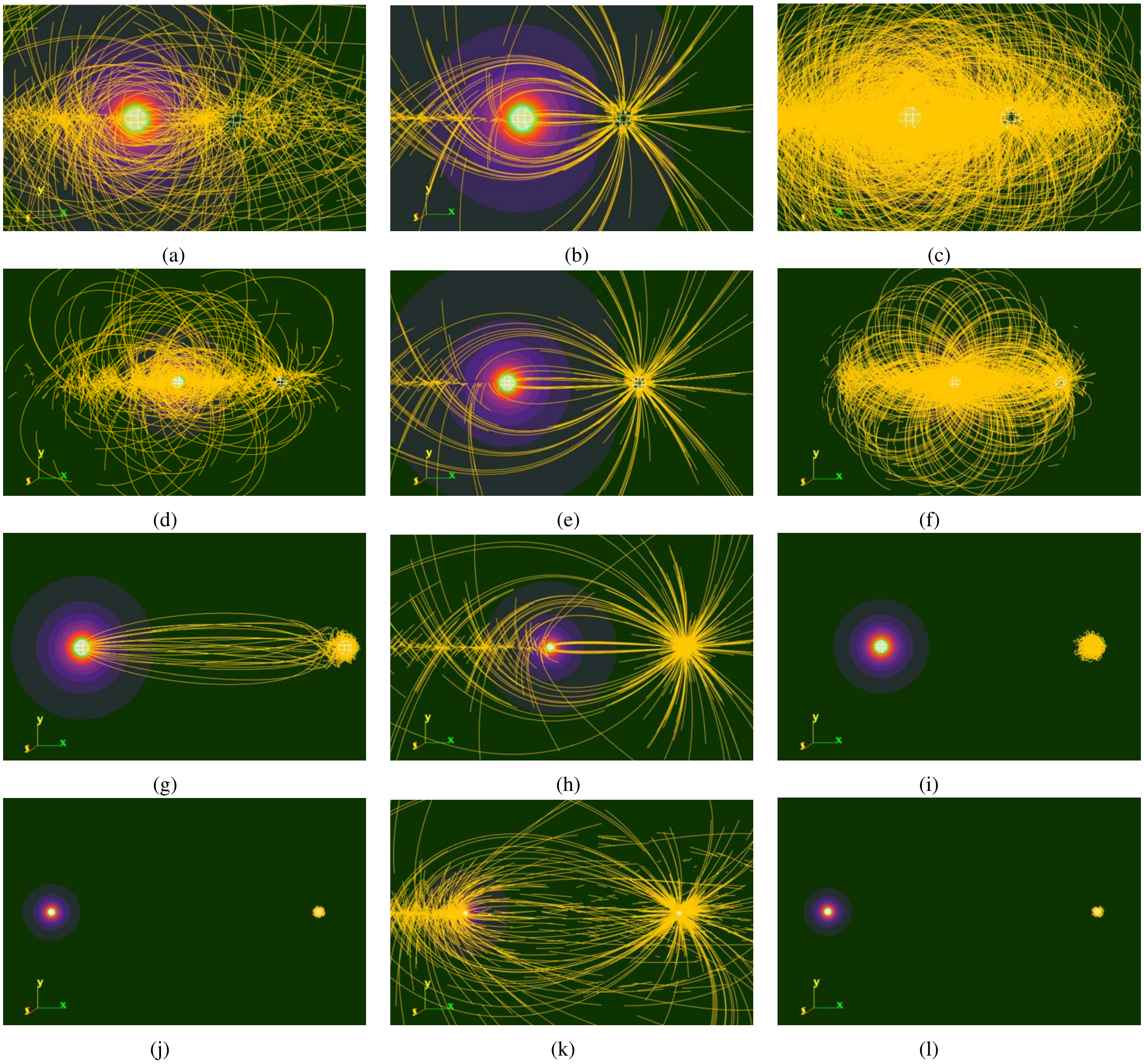

Fig. 19. Photoelectron trajectories from a 5.021-V, 1-m radius target (right) in sunlight at varying distances from a 1-kV, 1-m radius servicer (left) using nonlinear, Laplace, and Debye–Hückel potentials in space models. (a) 10-m separation, nonlinear model. (b) 10-m separation, Laplace model. (c) 10-m separation, Debye–Hückel model. (d) 20-m Separation, nonlinear model. (e) 20-m separation, Laplace model. (f) 20-m separation, Debye–Hückel model. (g) 40-m separation, nonlinear model. (h) 40-m separation, Laplace model. (i) 40-m separation, Debye–Hückel model. (j) 100-m separation, nonlinear model. (k) 100-m separation, Laplace model. (l) 100-m separation, Debye–Hückel model.

is proposed to measure the ambient environment and target's electron emissions, and the energy resolution $\Delta E/E$ is assumed to be 4%, comparable to the resolution found in [5]. The resolution is equivalent to the width of the discreet current bins measured by the RPA. The distribution of ambient electron current density to a positively charged spherical spacecraft as a function of velocity distribution in a Maxwellian plasma is [32], [52]

$$J(E_2) - J(E_1) = \frac{q_e n_e (1 + q_e V_s / k_B T_e)}{(2\pi m_e)^{1/2} (k_B T_e)^{3/2}} \int_{E_1}^{E_2} e^{-E/k_B T_e} E \mathrm{d}E \tag{14}$$

where V_s is the servicer potential and E is the electron energy, or $E = (1/2) m_e v_e^2$ assuming nonrelativistic particles. In addition, when electrons approach a positively charged spacecraft, they gain an energy equal to $q_e V_s$, which shifts the distribution versus energy plot $q_e V_s$ to the right [52]. This provides a method of determining the servicer potential using an RPA and must be considered when modeling the distribution.

As previously outlined, when conducting touchless potential sensing, the arrival energy of the emitted electrons at the servicer is approximately equal to the difference in potential between the servicer and target $E = q_e V_s - q_e V_t$. However, electrons are emitted with energies on the order of a few volts,

TABLE VIII

Measured Current Density of Tracked Electron Emissions in NASCAP-2k for All Simulations Discussed in Sections VIII-A and VIII-B

Separation distance (m)	**Photoelectron current density to 1kV servicer in sunlight $(\mathbf{A/m^2})$**	**Photoelectron current density to 10kV servicer in sunlight $(\mathbf{A/m^2})$**	**SEE current density to 1kV servicer in eclipse $(\mathbf{A/m^2})$**	**SEE current density to 10kV servicer in eclipse $(\mathbf{A/m^2})$**
10	1.998E-6	1.474E-6	5.804E-15	1.880E-15
20	1.092E-7	7.056E-7	4.420E-10	8.613E-14
40	2.327E-7	3.786E-7	1.030E-10	2.054E-13
100	0	0	9.239E-12	8.465E-11

as discussed in Section VIII, so the arrival energy may be more accurately represented as

$$E = (q_e V_s - q_e V_t) \int_0^\infty f(E_i) \mathrm{d}E_i \tag{15}$$

where $f(E_i)$ is the distribution of emission energies of an emitted particle species. Furthermore, because the incoming particles are accelerated to the potential of the servicer, the minimum energy measured is also equal to the potential of the servicer. Therefore, it is assumed that for a positive target, the arrival energy is equal to the potential of the servicer $E = q_e V_s \int_0^\infty f(E_i)\mathrm{d}E_i$. The distribution of secondary electron emission energies may be represented using the Chung–Everhart model, as mentioned in Section VIII [47]

$$f(E_s) = \frac{6\varphi^2 E_s}{(E_s + \varphi)^4} \tag{16}$$

where E_s is the energy of the emitted secondary electron with respect to the vacuum level. The emission energy of photoelectrons, based on lab tests, may be from 1 to 3 eV as previously mentioned, but the distribution within this range is not well known [32], [49]. Thus, the emission energy for this approximation is assumed to be negligible or $\int_0^\infty f(E_{ph}) = 1$.

The target's electron emissions current is superimposed on the ambient current, simulating the distribution of current densities measured by a servicer's RPA. The signal is assumed to be differentiable from the noise if it is approximately 1 nA larger than the ambient environment, based on [31].

A. Passive Touchless Potential Sensing

In order to determine whether passive touchless potential sensing is possible in the cislunar regions considered in this study, the tracked current density to the surface element of the servicer closest to the target, which will be referred to as the measured current density, is determined using NASCAP-2k's "Results" tab, shown in Table VIII. This simulates the current density that is received by an RPA pointed at the target, and the total current is determined by simply multiplying the current density by the area of the RPA. The measured photoelectron current density to the 10-kV servicer decreases as the separation distance increases. However, the measured photoelectron current density to the 1-kV servicer is larger at 40 m than at 20 m. This is likely because the emissions are attracted directly to the servicer rather than orbiting around the servicer and target, as shown in Fig. 17. In addition, the secondary electron emissions measured by the 10-kV servicer increase as the distance increases. This is because the total secondary electron emissions from the target decrease due to the acceleration of the electrons close to the highly positive servicer, as discussed in Section VIII-A. This trend is also seen for the 1-kV servicer for the separation distances from 10 to 40 m. However, the measured secondary electron emissions decrease from 40 to 100 m. This is because the total emissions remain approximately the same between these distances, as the target is mostly outside the influence of the servicer at 40 m of separation. Then, as the distance increases, less secondary electron emissions are pulled toward the positive servicer. Therefore, the optimal separation distance when measuring naturally emitted secondary electrons is near the outside edge of the servicer's potential sheath, and minimizing the separation distance when measuring photoelectrons is optimal.

The maximum current density for the sunlit cases occurs at 10 m of separation. The current measured by a 3-cm radius RPA at this separation distance is 5.6 and 4.1 nA for the 1- and 10-kV servicer, respectively, which is detectable. However, these measurements are not large enough to form a clearly distinguishable peak in RPA current measurements, as shown in Fig. 20. In order to determine whether there is a situation in which there is a distinct peak from passively emitted photoelectrons, the trajectories are tracked for a lower servicer potential case in NASCAP-2k, as this will decrease the measured ambient electron current density. The servicer is held to 50 V, and the target once again floats to 5.021 V with a photoelectron current density of 3.249E-6 A/m^2. The tracked current density to the servicer's surface element closest to the target is found to be 7.909E-7 A/m^2, and the measurement bins for a 3-cm radius RPA are shown in Fig. 21. The energy bin containing the measured photoemissions is approximately 2.37 nA and three times the maximum energy bin of the ambient environment, which is sufficient to differentiate it from the ambient environment. Therefore, lower servicer potentials are desirable when sensing the naturally emitted photoemissions from a target. However, this also decreases the effective Debye length of the servicer, so an optimization study may be conducted to determine the optimal conditions for passive potential sensing of a positively charged target in cislunar space regions with short Debye lengths. Measuring a distinct peak may also be more readily achieved through the use of an RPA with a finer energy resolution.

The maximum measured secondary electron current density from a negative target to the servicer is 1.030E-10 A/m^2, as shown in Table VIII. This requires an RPA with a radius of approximately 85 cm to measure an emitted current of 1 nA.

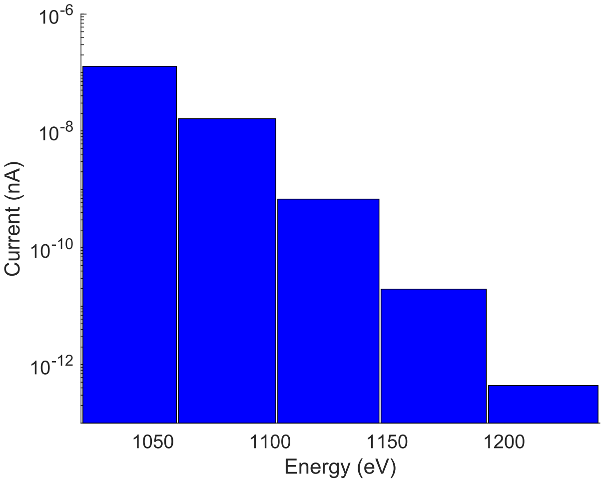

Fig. 20. Current measurement bins of passive photoemissions from a 5.021-V target to a 1-kV servicer at a separation distance of 10 m. Measurements are binned for a 3-cm radius RPA with an energy resolution $\Delta E/E$ of 4%.

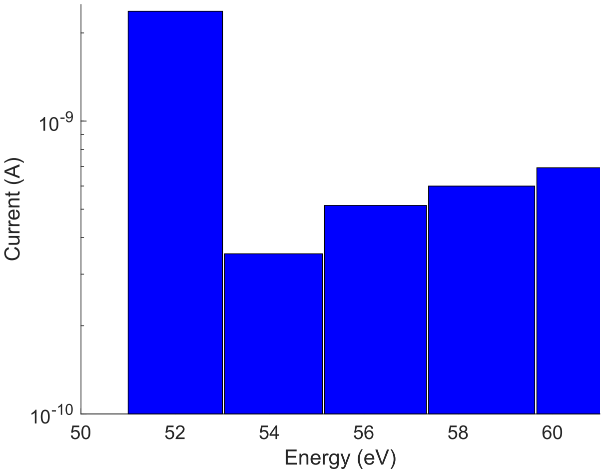

Fig. 21. Current measurement bins of passive photoemissions from a 5.021-V target to a 50-V servicer at a separation distance of 10 m. Measurements are binned for a 3-cm radius RPA with an energy resolution $\Delta E/E$ of 4%.

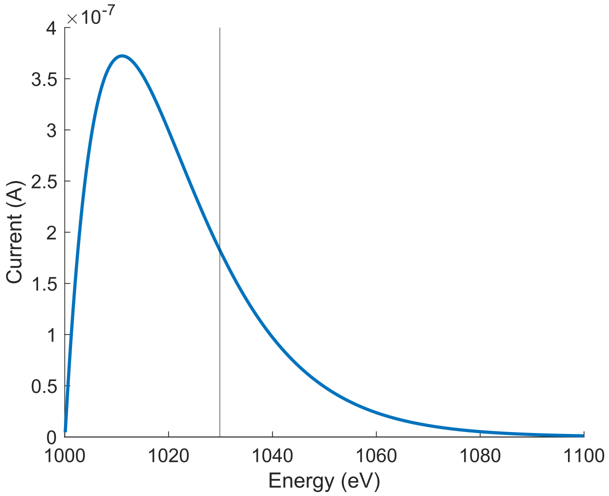

Fig. 22. Current distribution to an 85-cm radius RPA on a 1-kV servicer. The vertical black line marks the arrival energy expected from a target charged to −29.89 V.

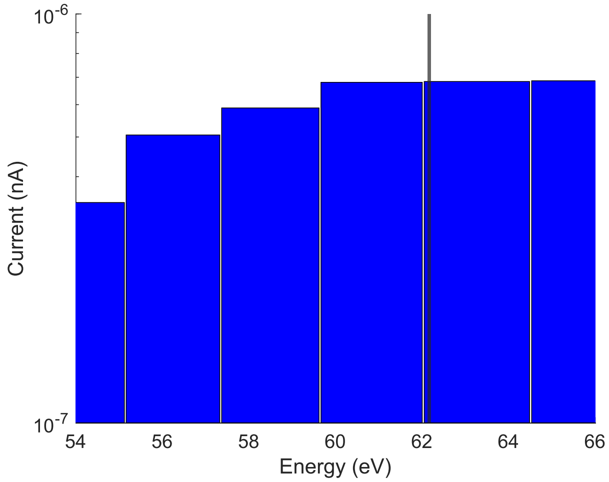

Fig. 23. Current measurement bins of passively emitted secondary electrons and ambient environment electrons to a 94-cm radius RPA on a 50-V servicer. The black vertical line marks the arrival energy expected from a target charged to −12.16 V. Measurements are binned for an RPA with energy resolution $\Delta E/E$ of 4%.

However, the current from the ambient environment given these conditions is on the order of 100 nA, two orders of magnitude larger than the current due to secondary electron emissions from the target, so there is no discernible peak in the current distribution due to secondary electron emissions from the target, as shown in Fig. 22. In order to determine whether minimizing the servicer potential may allow for detection of secondary electron emissions, a 2-m radius servicer and a 1-m radius target at a separation distance of 10 m are modeled in NASCAP-2k. The servicer is then held to 50 V, and the target floats to −12.16 V with a secondary electron current density of 3.123E-8 A/m^2. The trajectories are once again modeled, and the measured current density is found to be 3.621E-10 A. To measure 1 nA of current, a 94-cm radius RPA is required. However, the current from the ambient environment is on the order of 10 nA under these conditions, and there is again no discernible peak in distribution or RPA measurements, as shown in Fig. 23. In addition, the RPA radii required to detect the secondary electron current are several times larger than RPA used in previous experiments, which have radii on the order of a few centimeters [5], [53], and may not be physically feasible. Therefore, passive potential sensing using secondary electron emission from negatively charged spacecraft in eclipse in short Debye length regions around the moon is not feasible.

B. Active Touchless Potential Sensing

Two case studies are conducted to determine the feasibility of active touchless potential sensing in cislunar regions with short Debye lengths. Active potential sensing makes use of an electron beam or UV laser to excite secondary electrons or photoelectrons. This is not readily simulated in NASCAP-2k, so analytic expressions are utilized to determine the approximate potential of the servicer and target and secondary electron emissions excited when an electron beam is used to excite electron emissions. The current balance equation of a servicer emitting electrons through an electron beam is [32]

$$I_e(V)(1-\alpha) - I_i(V) - I_{\text{ph}}(V) - I_{e,B} = 0 \tag{17}$$

where I_e is the incident electron current, I_i is the incident ion current, α is the sum of the secondary electron yield δ and backscattered electron yield η, I_{ph} is photoelectron current, and $I_{e,B}$ is the electron beam current. It is assumed that the energy of the electron beam is higher than the energy of the servicer, so all electrons emitted from the beam escape the servicer. The orbit motion limited (OML) equations for spherical current collection are utilized, and the incident electron current is [32]

$$I_e = \frac{1}{4} q_e n_e v_e A \exp\left(\frac{q_e V}{k_B T_e}\right) \quad \text{for } V < 0 \tag{18a}$$

$$I_e = \frac{1}{4} q_e n_e v_e A \left(1 + \frac{q_e V}{k_B T_e}\right) \quad \text{for } V > 0 \tag{18b}$$

where A is the total surface area of the spacecraft. The incident ion current is

$$I_i = \frac{1}{4} q_e n_i v_i A \left(1 - \frac{q_e V}{k_B T_i}\right) \quad \text{for } V < 0 \tag{19a}$$

$$I_i = \frac{1}{4} q_e n_i v_i A \exp\left(\frac{-q_e V}{k_B T_i}\right) \quad \text{for } V > 0. \tag{19b}$$

The photoelectron current is

$$I_{\text{ph}} = q_e A_{\text{ph}} f Y_{\text{ph}} (1-R)\cos(\theta) \quad \text{for } V < 0 \tag{20a}$$

$$I_{\text{ph}} = q_e A_{\text{ph}} f Y_{\text{ph}} (1-R)\cos(\theta) \exp\left(\frac{-q_e V}{k_B T_{\text{ph}}}\right) \quad \text{for } V > 0 \tag{20b}$$

where A_{ph} is the sunlit area of the spacecraft, f is the flux of photons, Y_{ph} is the photoelectron yield or emitted photoelectron per incident photon, R is the reflectivity of the surface material, and θ is the impact angle. For this approximation, the impact angle is assumed to be zero, or perpendicular to the surface. The Ly–α line (10.2 eV) is dominant in the solar spectrum, and the flux of photons with energy equal to this is estimated as 4.48E17 photons/m^2/s from the NRLSSI2 reference spectra from July 2008. The yield and reflectance of aluminum at 10.2 eV and a 0° impact are 0.58 and 0.93, respectively [54].

The secondary electron yield δ depends on the incidence energy of the primary particle and angle of incidence. For this approximation, the incidence angle of the electrons is again assumed to be zero or perpendicular to the surface of the spacecraft, so δ can be roughly approximated by the Sanders and Inouye yield model [55]

$$\delta(E,0) = c\left[e^{-E/a} - e^{-E/b}\right] \tag{21}$$

where $a = 4.3\ E_{\max}$, $b = 0.367\ E_{\max}$, and $c = 1.37\delta_{\max}$ [51]. $\delta_{\max}$ is the maximum yield and $E_{\max}$ is the energy at the maximum yield. For aluminum, these values are assumed to be 0.97 and 300 eV [48].

The backscattered electron yield η for sufficiently high impact energies depends on the atomic number of the surface material Z and the impact angle. For this approximation, the incidence angle is once again assumed to be zero or perpendicular to the surface of the spacecraft, and the yield can be approximated by the model proposed in [55] and [56]

$$\eta(Z,0) = \frac{a - 1 + 0.5^a}{a+1} \tag{22}$$

with $a(Z) = 0.045Z$ being an experimentally fit parameter. The minimum electron energy (in eV) that makes this approach valid is shown to be

$$E_{\min} \geq 13.7 Z^{4/3} \tan(\theta/2) \tag{23}$$

with $180° - \theta$ being the deflection angle of the electron in the material. To establish this value, Romero-Calvo et al. [55] suggested using $\theta = 45°$. If the impact energy is smaller than the minimum energy, the backscattered electron current is assumed to be negligible. The atomic number of aluminum is 13 [48], resulting in a minimum energy of 173.46 eV.

Electron emissions escape from the surface with energies on the order of a few volts. Therefore, if the spacecraft is more than a few volts positive, the electron emissions will be attracted back toward the servicer. It is shown in Section VIII that a positively charged servicer may attract emissions away from the target even if it is positively charged, but this will be ignored for charging purposes. Furthermore, in order to find α in a Maxwellian plasma, the yield is integrated over the distribution function. As a result, the electron emission yield is modeled as

$$\alpha = \int_0^{\infty} (\eta(E) + \delta(E)) f_E(E) \quad \text{for } V < 0 \tag{24a}$$

$$\alpha = 0 \quad \text{for } V > 0 \tag{24b}$$

where $f_E(E)$ is the Maxwellian energy distribution function

$$f_E(E) = \frac{2E^{1/2}}{\pi^{1/2}(k_B T_e)^{3/2}} \exp\left(\frac{-E}{k_B T_e}\right). \tag{25}$$

The current balance equation of a target being impacted by an electron beam, assuming the entirety of the beam impacts the target, is [4], [32]

$$I_e(V)(1-\alpha) - I_i(V) - I_{\text{ph}}(V) + I_{e,B}(V)(1-\alpha_B) = 0 \tag{26}$$

where α_B is the sum of the secondary electron and backscattered electron emissions due to the beam. The effective impact energy of the electron beam is approximated as [32]

$$E_{\text{eff}} = E_B + q_e V_t - q_e V_s \text{ for } q_e V_s - q_e V_t < E_B \tag{27}$$

$$E_{\text{eff}} = 0 \text{ for } q_e V_s - q_e V_t \geq E_B \tag{28}$$

where E_B is the emission energy of the beam. If the difference between the potential of the servicer and the target is greater than the energy of the electron beam, the beam will be deflected by both objects and not impact the target [32]. The effective energy of the electron beam then serves as the impact energy when calculating the secondary electron and backscattered electron yield α_B. The secondary electron current excited by the electron beam is found as

$$I_{\text{SE,B}} = \delta(E_{\text{eff}}) I_{e,B}. \tag{29}$$

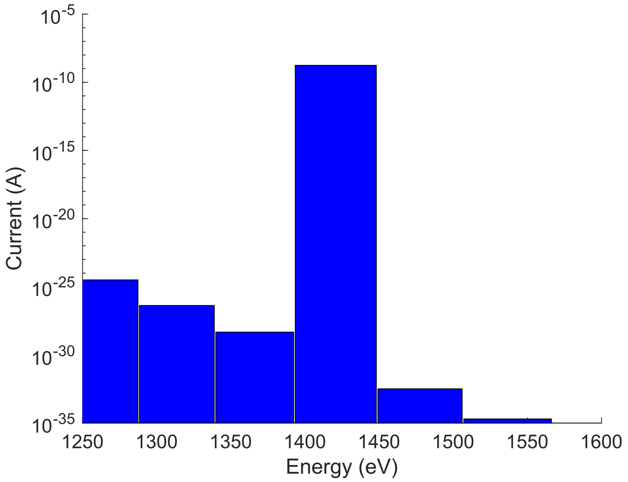

Fig. 24. Current measurement bins of actively emitted secondary electrons from a −647.78-V target to a 729.37-V servicer at a separation distance of 40 m. Measurements are binned for an RPA with an energy resolution $\Delta E/E$ of 4%.

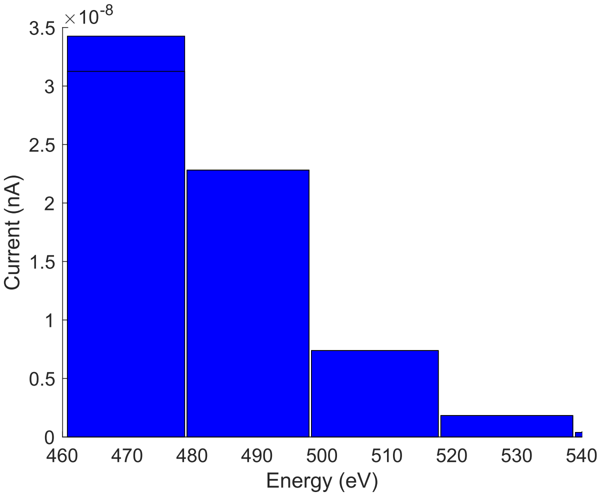

Fig. 25. Current measurement bins of actively emitted secondary electrons from a 4.306-V target to a 451.73-V servicer at a separation distance of 20 m. The black horizontal line in the first bin represents the current measured at that energy when no target emissions are detected. Measurements are binned for an RPA with an energy resolution $\Delta E/E$ of 4%.

Active charging is simulated for two scenarios. The first includes a 1-m radius servicer and target in eclipse with a 2-kV, 400-μA beam. The potentials of the servicer and target are found to be 729.37 and −647.78 V, respectively, and the secondary electron current excited by the beam is 3.261E-4A. In order to determine the current density to the servicer, the target and servicer are assumed to be separated by 40 m and the electron beam is assumed to have a divergence angle of 0.1°. The radius of the area of the target impacted by the electron beam is then approximately 7 cm. A circular surface element with a 7-cm radius is created on the surface of the target closest to the servicer in NASCAP-2k, and the secondary electron emissions are modeled from this area following the same process outlined in Section VIII. The measured current density is found as 6.194E-7 A/m^2 in NASCAP-2k or 1.8 nA when measured by a 3-cm radius RPA, and the measured current distribution is shown in Fig. 24. The temperature of the dayside solar wind electrons is 11 eV, so the distribution of ambient electrons at the energy of the measured target electron emissions, approximately 1,377 V, is negligible, as shown. Therefore, the target's emissions are easily identifiable, and active touchless potential sensing of a negative target in eclipse is feasible.

The second scenario includes a 1-m radius servicer and target in sunlight with a 0.5-kV, 250-μA beam. The potentials of the servicer and target are found to be 451.73 and 4.306 V, respectively, and the secondary electron current due to the beam is 0.114 mA. For this scenario, the servicer and target are assumed to be 20 m apart, and the electron beam is again assumed to have a divergence angle of 0.1°, resulting in an impact area with a radius of 14 cm. As stated previously, for charging purposes, the secondary electron current excited by the beam is assumed to be zero for a positive target. However, in Section VIII, it was found that the servicer may pull emissions from a positively charged target. Therefore, a representative circular surface element is once again created on the target, and the measured current density is 1.046E-6 A/m^2 or 3 nA when measured by a 3-cm radius RPA. The measured current bins are shown in Fig. 25, and the horizontal black line in the first bin represents the current measured when no emissions are detected from the target. As shown, there is a distinguishable change in peak when viewing the measured energy bins. Therefore, the current from the target may be differentiated from the ambient environment's current, and active touchless potential sensing of a positively charged spacecraft in short Debye length regions around the moon is feasible. For all passive and active sensing scenarios, an instrument with higher resolution or a collimator may be used to enhance the signal-to-noise ratio of the detector [57].

X. CONCLUSION

This article presents the solutions for the potential field surrounding a spherical spacecraft around the moon using the effective Debye length, determined using NASCAP-2k, SPIS, and turning point solutions. The effective Debye length varies between solution methods, which is found to provide an approximation of the range of potential fields. In addition, all methods show that the effective Debye length increases as the radius and potential of a spherical spacecraft increases, creating a larger sheath around a spherical servicer and enabling touchless potential sensing at larger separation distances than estimated with the electron Debye length. Deflections due to the magnetic field and collisions are found to be secondary considerations compared to the potential field damping, allowing interactions between a servicer and a target to be approximated using NASCAP-2k simulations. It is found that secondary electron emissions from a target decrease as it is approached by a servicer, as the ambient electrons are accelerated to energies higher than the optimal energy for emissions. Furthermore, if the servicer's potential field exceeds the potential of the target, the emissions from a positive target may be drawn toward the servicer and detected.

It is revealed that active touchless potential sensing and passive potential sensing of photoelectrons is feasible in cisluanr regions with short Debye lengths. Touchless potential sensing may then be extended to this region, so long as care is considered for potential shielding that will occur.

ACKNOWLEDGMENT

The authors thank Dr. Álvaro Romero-Calvo for the fruitful discussion and his comments on the manuscript and Dr. David Cooke for his insights.

REFERENCES

[1] M. Bengtson, K. Wilson, J. Hughes, and H. Schaub, "Survey of the electrostatic tractor research for reorbiting passive GEO space objects," *Astrodynamics*, vol. 2, no. 4, pp. 291–305, Dec. 2018.

[2] E. A. Hogan and H. Schaub, "Impacts of tug and debris sizes on electrostatic tractor charging performance," *Adv. Space Res.*, vol. 55, no. 2, pp. 630–638, 2015.

[3] E. A. Hogan and H. Schaub, "Impacts of hot space plasma and ion beam emission on electrostatic tractor performance," *IEEE Trans. Plasma Sci.*, vol. 43, no. 9, pp. 3115–3129, Sep. 2015.

[4] E. A. Hogan and H. Schaub, "Space weather influence on relative motion control using the touchless electrostatic tractor," *J. Astron. Sci.*, vol. 63, no. 3, pp. 237–262, 2016.

[5] M. T. Bengtson, K. T. Wilson, and H. Schaub, "Experimental results of electron method for remote spacecraft charge sensing," *Space Weather*, vol. 18, no. 3, pp. 1–12, Mar. 2020.

[6] A. R. Calvo, J. Hammerl, and H. Schaub, "Touchless potential sensing of complex differentially-charged shapes using secondary electrons," in *Proc. AIAA SCITECH*, 2022, p. 2311.

[7] K. Wilson and H. Schaub, "X-ray spectroscopy for electrostatic potential and material determination of space objects," *IEEE Trans. Plasma Sci.*, vol. 47, no. 8, pp. 3858–3866, Aug. 2019.

[8] K. T. Wilson, M. T. Bengtson, and H. Schaub, "X-ray spectroscopic determination of electrostatic potential and material composition for spacecraft: Experimental results," *Space Weather*, vol. 18, no. 4, Apr. 2020, Art. no. e2019SW002342.

[9] A. R. Calvo, K. Champion, and H. Schaub, "Enabling ultraviolet lasers for touchless spacecraft potential sensing," *IEEE Trans. Plasma Sci.*, pp. 1–15, 2023.

[10] K. Wilson and H. Schaub, "Impact of electrostatic perturbations on proximity operations in high earth orbits," *J. Spacecraft Rockets*, vol. 58, no. 5, pp. 1293–1302, Sep. 2021.

[11] K. Wilson, A. Romero-Calvo, and H. Schaub, "Constrained guidance for spacecraft proximity operations under electrostatic perturbations," *J. Spacecraft Rockets*, vol. 59, no. 4, pp. 1304–1316, Jul./Aug. 2022.

[12] H. Schaub, G. G. Parker, and L. B. King, "Challenges and prospects of Coulomb spacecraft formation control," *J. Astron. Sci.*, vol. 52, nos. 1–2, pp. 169–193, Mar. 2004.

[13] F. Casale, H. Schaub, and J. D. Biggs, "Lyapunov optimal touchless electrostatic detumbling of space debris in GEO using a surface multisphere model," *J. Spacecraft Rockets*, vol. 58, no. 3, pp. 764–778, May 2021.

[14] H. Schaub and D. F. Moorer, "Geosynchronous large debris reorbiter: Challenges and prospects," *J. Astron. Sci.*, vol. 59, nos. 1–2, pp. 161–176, 2012.

[15] T. Zhang, Y. Sun, and Z. Tang, "3D visualization of solar wind ion data from the Chang'E-1 exploration," *Comput. Geosci.*, vol. 37, no. 10, pp. 1711–1718, Oct. 2011. [Online]. Available: https://www.sciencedirect.com/science/article/pii/S0098300411001130

[16] V. Angelopoulos, "The ARTEMIS mission," in *The ARTEMIS mission*. New York, NY, USA: Springer, 2010, pp. 3–25.

[17] E. M. Willis, H. F. Haviland, J. I. Minow, and V. N. Coffey, "A comparison of ARTEMIS data with the lunar plasma design environment for NASA crewed missions," in *Proc. Appl. Space Environ. Conf.*, 2019, pp. 1–4.

[18] NASA. (2022). *NASA Strategic Plan 2022*. [Online]. Available: https://www.nasa.gov/sites/default/files/atoms/files/fy_22_strategic_plan.pdf

[19] C. R. Seubert, L. A. Stiles, and H. Schaub, "Effective Coulomb force modeling for spacecraft in earth orbit plasmas," *Adv. Space Res.*, vol. 54, no. 2, pp. 209–220, 2014.

[20] H. Schaub and L. E. Z. Jasper, "Orbit boosting maneuvers for two-craft Coulomb formations," *J. Guid., Control, Dyn.*, vol. 36, no. 1, pp. 74–82, Jan. 2013.

[21] F. B. Leahy, "SLS-SPEC-159, cross-program design specification for natural environments (DSNE)," Nat. Aeronaut. Space Admin., Washington, DC, USA, Tech. Rep. M20-7865 / SLS-SPEC-159, 2021.

[22] S. Guillemant, V. Génot, J.-C. Matéo-Vélez, R. Ergun, and P. Louarn, "Solar wind plasma interaction with solar probe plus spacecraft," *Ann. Geophys.*, vol. 30, no. 7, pp. 1075–1092, 2012.

[23] L. A. Stiles, H. Schaub, K. K. Maute, and D. F. Moorer, "Electrostatically inflated gossamer space structure voltage requirements due to orbital perturbations," *Acta Astronautica*, vol. 84, pp. 109–121, Mar. 2013.

[24] N. Murdoch, D. Izzo, C. Bombardelli, I. Carnelli, A. Hilgers, and D. Rodgers, "Electrostatic tractor for near earth object deflection," in *Proc. 59th Int. Astron. Congr.*, vol. 29, 2008, pp. 1–11.

[25] J. S. Halekas, Y. Saito, G. T. Delory, and W. M. Farrell, "New views of the lunar plasma environment," *Planetary Space Sci.*, vol. 59, no. 14, pp. 1681–1694, 2011.

[26] V. L. Pisacane, *The Space Environment and its Effects on Space Systems*. Reston, VA, USA: American Institute of Aeronautics and Astronautics, 2008.

[27] H. Zhang et al., "Three-dimensional lunar wake reconstructed from ARTEMIS data," *J. Geophys. Res., Space Phys.*, vol. 119, no. 7, pp. 5220–5243, 2014.

[28] V. Davis, M. Mandell, D. Cooke, and D. Ferguson, "Semi-analytic and PIC (particle-in-cell) methods for quantifying charging in dense, cold plasma," in *Proc. 13th Spacecraft Charging Technol. Conf.*, Pasadena, CA, USA, 2014, pp. 23–27.

[29] B. Thiébault, "Potential barrier in the electrostatic sheath around a magnetospheric spacecraft," *J. Geophys. Res.*, vol. 109, no. 12, pp. 1–11, 2004.

[30] E. A. Hogan and H. Schaub, "General high-altitude orbit corrections using electrostatic tugging with charge control," *J. Guid., Control, Dyn.*, vol. 38, no. 4, pp. 699–705, 2015.

[31] M. Bengtson, J. Hughes, and H. Schaub, "Prospects and challenges for touchless sensing of spacecraft electrostatic potential using electrons," *IEEE Trans. Plasma Sci.*, vol. 47, no. 8, pp. 3673–3681, Aug. 2019.

[32] S. T. Lai, *Fundamentals of Spacecraft Charging: Spacecraft Interactions With Space Plasmas*. Princeton, NJ, USA: Princeton Univ. Press, 2012.

[33] J. G. Laframboise and L. W. Parker, "Probe design for orbit-limited current collection," *Phys. Fluids*, vol. 16, no. 5, pp. 629–636, 1973.

[34] V. Davis, B. Gardner, and M. Mandell, "NASCAP-2K version 4.3 users manual," Leidos Holdings San Diego, CA, USA, Tech. Rep. AFRL-RV-PS-TR-2017-0002, 2016.

[35] V. Davis and M. Mandell, "NASCAP-2K version 4.3 scientific documentation," Leidos, San Diego CA, USA, Tech. Rep. AFRL-RV-PS-TR-2017-0001, 2016.

[36] P. Sarrailh et al., "SPIS 5: New modeling capabilities and methods for scientific missions," *IEEE Trans. Plasma Sci.*, vol. 43, no. 9, pp. 2789–2798, Sep. 2015.

[37] S. Hess et al., "Spacecraft plasma interactions network in Europe (SPINE)," European Union, Tech. Rep. ESA-SPIS-GEO-D7-SUM-2013-03-001, 2021.

[38] V. Davis et al., "Validation of NASCAP-2K spacecraft-environment interactions calculations," in *Proc. 8th Spacecraft Charging Technol. Conf.*, 2004, pp. 1–19.

[39] K. B. Blodgett, "Currents limited by space charge between concentric spheres," in *Thermionic Phenomena*. Amsterdam, The Netherlands: Elsevier, 1961, pp. 125–135.

[40] N. F. Ness, "Interaction of the solar wind with the moon," in *Solar-Terrestrial Physics/1970* (Astrophysics and Space Science Library). Berlin, Germany: Springer, 1972, pp. 347–393.

[41] D. Knipp, *Understanding Space Weather and the Physics Behind It* (Space Technology Series). New York, NY, USA: McGraw-Hill, 2011.

[42] E. P. Romashets, S. Poedts, and M. Vandas, "Modeling of the magnetic field in the magnetosheath region," *J. Geophys. Res., Space Phys.*, vol. 113, no. 2, pp. 1–15, Feb. 2008. [Online]. Available: https://agupubs.onlinelibrary.wiley.com/doi/abs/10.1029/2006JA012072

[43] E. Lucek et al., "The magnetosheath," *Space Sci. Rev.*, vol. 118, no. 1, pp. 95–152, 2005.

[44] A. Y. Alksne and D. L. Webster, "Magnetic and electric fields in the magnetosheath," *Planet. Space Sci.*, vol. 18, no. 8, pp. 1203–1212, Aug. 1970.

[45] G. Livadiotis, "Collision frequency and mean free path for plasmas described by Kappa distributions," *AIP Adv.*, vol. 9, no. 10, Oct. 2019, Art. no. 105307, doi: 10.1063/1.5125714.

[46] J. Greenwood, "The correct and incorrect generation of a cosine distribution of scattered particles for Monte-Carlo modelling of vacuum systems," *Vacuum*, vol. 67, no. 2, pp. 217–222, Sep. 2002.

[47] M. S. Chung and T. E. Everhart, "Simple calculation of energy distribution of low-energy secondary electrons emitted from metals under electron bombardment," *J. Appl. Phys.*, vol. 45, no. 2, pp. 707–709, 1974.

[48] D. R. Lide, *CRC Handbook of Chemistry and Physics*, 84th ed. Boca Raton, FL, USA: CRC Press, 2003.

[49] S. T. Lai and M. F. Tautz, "Aspects of spacecraft charging in sunlight," *IEEE Trans. Plasma Sci.*, vol. 34, no. 5, pp. 2053–2061, Oct. 2006.

[50] H. Schaub and Z. Sternovsky, "Active space debris charging for contactless electrostatic disposal maneuvers," *Adv. Space Res.*, vol. 53, no. 1, pp. 110–118, Jan. 2013. [Online]. Available: https://www.sciencedirect.com/science/article/pii/S0273117713006364

[51] N. L. Sanders and G. T. Inouye, "Secondary emission effects on spacecraft charging: Energy distribution considerations," in *Proc. Spacecraft Charging Technol.*, 1978, pp. 747–755.

[52] S. T. Lai and C. Miller, "Retarding potential analyzer: Principles, designs, and space applications," *AIP Adv.*, vol. 10, no. 9, Sep. 2020, Art. no. 095324.

[53] K. Wilson, Á. Romero-Calvo, M. Bengtson, J. Hammerl, J. Maxwell, and H. Schaub, "Development and characterization of the ECLIPS space environments simulation facility," *Acta Astronautica*, vol. 194, pp. 48–58, May 2022.

[54] B. Feuerbacher and B. Fitton, "Experimental investigation of photoemission from satellite surface materials," *J. Appl. Phys.*, vol. 43, no. 4, pp. 1563–1572, 1972.

[55] A. Romero-Calvo, K. Champion, and H. Schaub, "Touchless spacecraft potential sensing using energetic electron beams and active photoemissions," in *Proc. 16th Spacecraft Charging Technol. Conf.*, 2022, pp. 1–8, Paper TPS15137.

[56] T. E. Everhart, "Simple theory concerning the reflection of electrons from solids," *J. Appl. Phys.*, vol. 31, no. 8, pp. 1483–1490, Aug. 1960.

[57] R. B. Torbert et al., "The electron drift instrument for MMS," *Space Sci. Rev.*, vol. 199, no. 1, pp. 283–305, Mar. 2016.

Kaylee Champion received the B.S. degree in aerospace engineering from The University of Texas at Austin, Austin, TX, USA, in 2021. She is currently pursuing the Ph.D. degree in astrodynamics with the Autonomous Vehicles Systems (AVS) Laboratory, University of Colorado at Boulder, Boulder, CO, USA.

She received the National Science Foundation Fellowship in 2021 and the NSTGRO Fellowship in 2022. Her current research interests include charged astrodynamics, spacecraft–plasma interactions, and mitigating space debris.

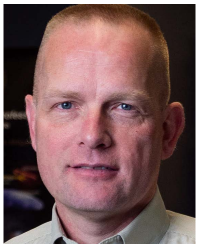

Hanspeter Schaub is currently a Professor and the Chair of the Aerospace Engineering Sciences Department, University of Colorado at Boulder, Boulder, CO, USA. He holds the Schaden Leadership Chair. He has over 28 years of research experience, of which four years are at Sandia National Laboratories, Albuquerque, NM, USA. His research interests are in astrodynamics, relative motion dynamics, charged spacecraft motion, as well as spacecraft autonomy. This has led to about 208 journal and 326 conference publications, as well as a 4th edition textbook on analytical mechanics of space systems. He has been the ADCS lead in the CICERO mission and the ADCS algorithm lead on a Mars mission and supporting ADCS for a new asteroid mission.

Mr. Schaub is a fellow of American Institute of Aeronautics and Astronautics (AIAA) and American Astronomical Society (AAS). He received the AIAA/ASEE Atwood Educator Award, the AIAA Mechanics and Control of Flight Award, and the Collegiate Educator of the Year for the AIAA Rocky Mountain Section. He has been awarded the H. Joseph Smead Faculty Fellowship, the Provost's Faculty Achievement Award, the Faculty Assembly Award for excellence in teaching, and the Outstanding Faculty Advisor Award.